From *operando* Raman mechanochemistry to "NMR crystallography": understanding the structures and interconversion of Zn-terephthalate networks using selective ^{17}O-labelling.

César Leroy[1,*], Thomas-Xavier Métro[2], Ivan Hung[3], Zhehong Gan[3], Christel Gervais[4] & Danielle Laurencin[1,*]

[1]ICGM, Univ Montpellier, CNRS, ENSCM, Montpellier, France

[2]IBMM, Univ Montpellier, CNRS, ENSCM, Montpellier, France

[3]National High Magnetic Laboratory (NHMFL), Tallahassee, Florida, USA

[4]Laboratoire de Chimie de la Matière Condensée de Paris (LCMCP), UMR 7574, Sorbonne Université, CNRS, Paris, France

e-mail : cesar.leroy@umontpellier.fr & danielle.laurencin@umontpellier.fr

Abstract

The description of the formation, structure and reactivity of coordination networks and MOFs remains a real challenge in a number of cases. This is notably true for compounds composed of Zn^{2+} ions and terephthalate ligands (benzene 1,4-dicarboxylate, BDC), because of the difficulties in isolating them as pure phases and/or because of the presence of structural defects. Here, using mechanochemistry in combination with *operando* Raman spectroscopy, the observation of the formation of various zinc-terephthalate compounds was rendered possible, allowing the distinction and isolation of three intermediates during the ball-milling synthesis of $Zn_3(OH)_4(BDC)$. An "NMR crystallography" approach was then used, combining solid-state NMR (^1H, ^{13}C and ^{17}O) and DFT calculations, in order to refine the poorly described crystallographic structures of these phases. Particularly noteworthy are the high-resolution ^{17}O NMR analyses, which were made possible in a highly efficient and cost-effective way, thanks to the selective ^{17}O-enrichment of either hydroxyl or terephthalate groups by ball-milling. This allowed the presence of defect sites to be identified for the first time in one of the phases, and the nature of the H-bonding network of the hydroxyls to be established in another. Lastly, the possibility of using deuterated precursors (*e.g.* D_2O and d_4-BDC) during ball-milling is also introduced, as a means for observing specific transformations during *operando* Raman spectroscopy studies, that would not have been possible with hydrogenated equivalents. Overall, the synthetic and spectroscopic approaches developed herein are expected to push forward the understanding of the structure and reactivity of other complex coordination networks and MOFs.

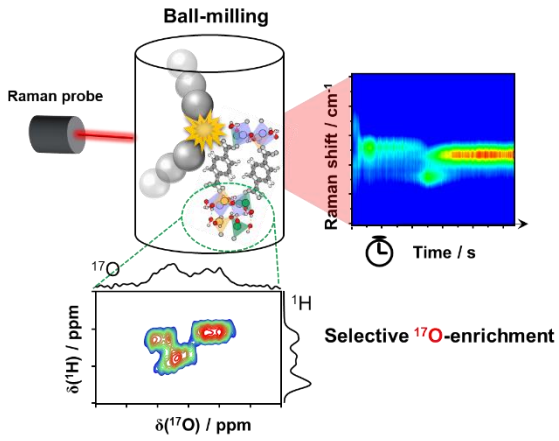

Introduction

In recent years, the use of mechanochemistry in molecular and materials synthesis has undergone an exponential development thanks to its increasing range of applications. Ball-milling (BM) syntheses have notably proved to be of great interest in pharmaceutics materials screening, battery development or even catalysis.[1], [2] More than offering a drastic reduction of bulk-solvent use/utilisation in the syntheses, it offers a precise control over the stoichiometry of the reaction, as well as simple and straightforward synthetic procedures.[3], [4] However, because of the closed environment of mechanochemical reactions (especially when conducted in stainless-steel jars), these syntheses are still considered as "black boxes". In this context, the last decade has seen the emergence of *in situ* time resolved analysis techniques applied to BM syntheses, which allow the evolution of the reaction medium to be monitored without needing to interrupt the milling process and open the jar. Among them, two are of particular interest: powder X-Ray Diffraction (pXRD) and Raman spectroscopy.[5]–[11] While the first requires the use of a synchrotron beamline, the second can be set-up in standard laboratories thanks to bench-top Raman spectrometers and probes. Such systems permit reaction rates to be followed, complex reaction schemes to be understood, and can also shed light on the appearance of yet unknown / unobserved reaction intermediates.[12], [13] Furthermore, these experimental installations can also be coupled with thermal imaging cameras, in order to have an even more precise description of the course of the chemical reactions.[14], [15] It is worth mentioning that some meticulous kinetic studies from *operando* Raman spectroscopy experiments have been recently proposed.[16], [17]

Metal-organic-frameworks (MOFs) represent an important family of porous materials, with porosities which can exceed 50% of their volume. The impressive range of their applications extends from fuel/gas storage to catalysis or even cancer therapy.[18]–[20] Various synthetic routes have been developed for obtaining and/or shaping these materials, like solvothermal or microwave syntheses, and also mechanochemistry.[21]–[24] The numerous properties of MOFs being strongly and directly related to their crystallographic structures, it is then of primary importance to precisely control their synthesis in order to obtain pure phases through meticulous and reproducible procedures.[25] In this context, *in situ* monitoring experiments can help observe or even trap interesting intermediates. For example, recently,

Jones *et al.* presented the use of *in situ* ^{1}H liquid state NMR for observing the formation of a Ni-MOF.[26] Insights into the nucleation and crystal growth processes of this MOF were obtained through the kinetic studies carried out at different temperatures. Concerning MOFs formed by mechanosynthesis, a recent example by Karadeniz *et al.* revealed the interplay between MOF-525 and its polymorph PCN-223, two porphyrinic zirconium MOFs. In their case, *in situ* pXRD monitoring allowed the MOF-525 to be detected as an intermediate during the formation of PCN-223, depending on the synthesic conditions used.[27] A similar experimental procedure also allowed the presence of metastable MOFs in the formation of *dia*-$Zn(MeIm)_2$ (MeIm : 2-methylimidazole) to be demonstrated.[6]

Among MOFs, those based on zinc (Zn-MOFs) have been the focus of much interest because of their high porosity and/or interesting applications. Indeed, zinc is a biocompatible metal that makes zinc materials, such as the porous scaffold Zn-xWE43 (WE43 being a Mg alloy) or the $Zn_2(BDC)_2$(diazabicyclooctane) MOF (with BDC standing for 1,4-benzenedicarboxylate) good candidates for implants and drug delivery.[28], [29] Furthermore, Zn-MOFs have shown great potential for applications as catalysts, anodes for lithium batteries, or materials for uranium adsorption/detection.[30]–[32] Among the numerous Zn-MOFs described to date, coordination complexes based on Zn^{2+}-dicarboxylate motifs have been found to exist as a very broad diversity of structures. For instance, the well-known structure of MOF-5 ($Zn_4O(BDC)_3$) exhibits four-fold coordinated zinc sites with bridging carboxylate functions, while MOF-2 ($Zn_2(BDC)_2$) presents one five-fold coordinated zinc with four bridging oxygens from carboxylate ligands and one additional coordinated water-molecule.[33], [34] Interconversion between these two structures has also been demonstrated in specific synthetic conditions (high pressure, temperatures up to 120°C).[35] Furthermore, the different investigations performed so far on coordination networks involving Zn^{2+} ions and terephthalate ligands (noted Zn-BDC from hereon), have enabled many other structures to be described, *e.g.*, $Zn(BDC)(H_2O)$,[36] $Zn_3(OH)_4(BDC)\cdot 6H_2O$,[37] and $(Zn_3(BDC)_4\cdot 4H_2O)_n$,[38], just to name a few. Here, we decide to focus our attention on four other Zn-BDC structures: a di-hydrated zinc

terephthalate coordination polymer, $Zn(BDC)(H_2O)_2$,[39] and three lamellar phases involving terephthalate and hydroxyl ligands (see **Table 1**).

Table 1: Zn-BDC compounds studied in this contribution, together with structural details, as initially reported in the corresponding references [40]–[43].

	ZTA1	ZTA2a	ZTA2b	ZTA3
Designation	ZTA1	ZTA2a	ZTA2b	ZTA3
CCDC code(s)	**DIKQET / 133475**	**ECATIO / 1520407** **PUCYA01**	**PUCYAO / 695449**	**PEKGAO / 295966**
Reference	[40]	[41]	[42]	[43]
Reported formula	$Zn(BDC)(H_2O)_2$	$Zn_2(OH)_2(BDC)$	$Zn_2(OH)_2(BDC)$	$Zn_3(OH)_4(BDC)$
Space Group	C2/c	C2/c	$P2_1/c$	C2/c
Representation	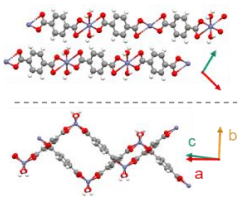	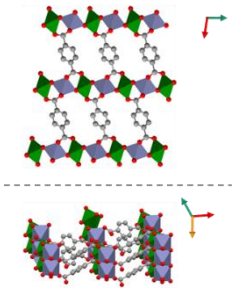	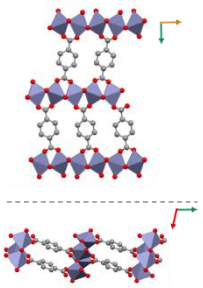	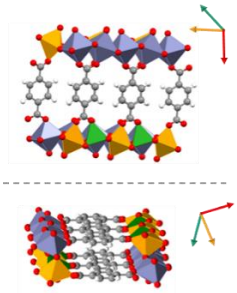
Metal centre geometry	Zn – Tetracoordinate	**Zn1** – Hexacoordinate **Zn2** – Hexacoordinate	Zn – Pentacoordinate	**Zn1** – Tetracoordinate **Zn2** – Pentacoordinate **Zn3** – Hexacoordinate
BDC ligands & coordination	1 carboxylate environment Monodentate	1 carboxylate environment Bridging	1 carboxylate environment Bridging	2 carboxylate environments Bridging
Remarks	- Zig-zag Chain - 2 coordinated-H_2O - Coordination polymer	- Lamellar - 1 hydroxyl environment - No information on crystal preparation	- Lamellar - 1 hydroxyl environment - No hydrogen position reported	- Lamellar - 4 hydroxyl environments - No hydroxyl hydrogens positions reported

The $Zn(BDC)(H_2O)_2$ phase (noted here **ZTA1**) consists of a "zig-zag" arrangement of chains formed by distorted tetrahedral zinc environments, in which each Zn^{2+} ion is linked to two monodentate BDC ligands, and two water molecules (**Table 1**). Regarding the three lamellar structures, two are polymorphs of general formula $Zn_2(OH)_2(BDC)$ (noted here **ZTA2a** and **ZTA2b**). The structure of the latter polymorph (**ZTA2b**) has been more thoroughly described so far:[42] it exhibits only one penta-coordinated zinc environment, with well-ordered π-stacked BDC units. The structure of the other polymorph (**ZTA2a**), *a contrario*, reveals more uncertainties. In fact, although several articles have

reported this phase (by looking at pXRD data), no consensus has been found in the literature about its structure. Rodriguez *et al.* attributed this compound to a distorted MOF-5 phase, caused by a default in one of the binding modes of carboxylate groups to Zn^{2+}.[44] Thirumurugan and Rao observed this phase as an intermediate in their hydrothermal reactions when using a Zn/BDC 1/1 molar ratio but were not able to propose an exact formula for it.[45] Hirai *et al.* were unable to isolate a pure phase of this material, but were able to detect it in a microwave synthesis when using a Zn/BDC ratio of 2/1 and working at specific pH (between 5.7 and 4.9).[37] In 2016, a crystal structure was reported in the Cambridge crystallography database (CCDC ECATIO), that matches the pXRD pattern of this same phase, and corresponds to the $Zn_2(OH)_2(BDC)$ chemical formula (with a Zn/BDC ratio of 2/1). Unfortunately, no information on its synthesis could be found.[41] When looking at the crystallographic file, it appears that it corresponds to a lamellar structure with two distinct zinc sites in octahedral geometry, which are separated by one bridging oxygen belonging to a hydroxyl (**Table 1**). Between two layers, the BDC ligands exhibit a "zig-zag" configuration of the aromatic rings. Hence, both polymorphs differ by subtle modifications of the BDC arrangements, resulting in different coordination modes of the metal centres, and the **ZTA2a** phase displays a slightly smaller interlamellar spacing than **ZTA2b** (about 10.1 Å *vs.* 10.8 Å, respectively) (see **Table 1**). Lastly, the fourth phase of interest in this work is $Zn_3(OH)_4(BDC)$ (noted **ZTA3**).[43] This other lamellar hydroxide terephthalate is formed in a 3/1 Zn/BDC stoichiometry. Three distinct zinc environments were reported to be present in the Zn-O polyhedra layers (with tetra/penta/hexa–coordination, according to the initially reported crystallographic file), which are connected to each other through terephthalate and hydroxyl anions.

Diffraction techniques remain, at the moment, the most common analytical tool to obtain structural information on Zn-BDC MOFs. However, preparing good quality crystals can be very challenging. Moreover, providing exact positions for hydrogen atoms from pXRD data remains an issue, and only 2 out of the 4 reported structures in **Table 1** fully report hydrogen positions (aromatics and hydroxyls/water). In complement to XRD, chemical and structural information on these phases can also be obtained through FTIR spectroscopy. For example, the O-H stretching modes of hydroxyls and water molecules are easily observed above 3000 cm^{-1}, and can inform on the H-bond networks in presence.

Moreover, the C-O stretching modes of carboxylate groups are identified by the presence of asymmetric and symmetric vibrations (noted $\nu_{as}(COO^-)$ and $\nu_s(COO^-)$, respectively) between 1650 – 1540 and 1450 – 1360 cm^{-1}, respectively, and information on the binding mode of the carboxylate ligands to zinc metal centres can *a priori* be proposed on the basis of the difference in wavenumbers between these two frequencies ($\Delta = \nu_{as}(COO^-)-\nu_s(COO^-)$).[46], [47] Surprisingly, very few articles have used solid state NMR (ssNMR) techniques to probe the local environment of the atoms in Zn-BDC structures, even for some of the more readily observable isotopes such as ^1H and ^{13}C.[36], [48]–[50] More generally speaking, numerous debates, some of which will be discussed more extensively later in this contribution, still remain about such zinc structures and their intermediates.

In order to help further elucidate the details of the structure of these phases, ^{17}O ssNMR is a very attractive tool. Oxygen-17 is a spin-5/2 quadrupolar nucleus of low natural abundance (0.04%), which presents a very wide chemical shift range (exceeding 1000 ppm), and also a very wide variation of quadrupolar interaction (QI) parameters (C_Q, η_Q). Moreover, recent investigations have shown that ^{17}O ssNMR spectroscopy can be of high interest for determining the binding mode of oxygen-ligands in coordination polymers and MOFs.[51]–[54] For example, Martins *et al.* have shown the powerful use of ultra-high field ^{17}O ssNMR experiments (35.2 T) applied on ^{17}O-enriched Mg and Al MOFs (α-$Mg_3(HCOO)_6$ and MIL53(Al)). Impressively, they were able to distinguish up to 12 inequivalent oxygen sites for as-made and activated phases of α-$Mg_3(HCOO)_6$.[55] Moreover, thanks to our recent developments of cost-efficient ^{17}O-labelling schemes using mechanochemistry,[53], [56], [57] including for carboxylic ligands like terephthalic acid,[58] the possibility to use such non-routine NMR analyses for the study of Zn-BDC structures as the ones in **Table 1** now becomes accessible.

In this contribution, we report a detailed investigation of the structure and interconversion between the four aforementioned Zn-BDC systems (**ZTA1**, **ZTA2a**, **ZTA2b** and **ZTA3**) synthesized using mechanochemistry. We first show how by modifying the initial stoichiometry of the reaction, and carefully monitoring the course of the BM reactions using *operando* Raman spectroscopy and thermal analysis of the milling jar, each of these different phases can be easily isolated in a pure form, and subsequently studied by *ex situ* methods (FTIR, powder X-ray diffraction, multinuclear ssNMR),

allowing further information about their structures to be gained. Moreover, we then demonstrate for the first time how, by using this synthetic methodology, it becomes possible to perform *selective* ^{17}O isotopic labelling of the different types of oxygen environments in such MOF structures (by enriching either the water/hydroxyl ligands, or the carboxylate ones), thereby opening the way to a level of structural insight which had not been achieved before. Lastly, we show how the combination of high-resolution ^{17}O NMR analysis of these compounds, and *ab initio* calculations of NMR parameters using the gauge-including projector augmented wave method (GIPAW), can improve and/or correct the structural models of these phases, thereby paving the way to other investigations on complex coordination networks and MOFs.

Experimental

Reagents

The following commercial precursors were used as received without further purification: terephthalic acid ($C_8H_6O_4$, Janssen Chemicals, 98% purity, noted here H_2BDC), deuterated terephthalic acid ($C_8D_4H_2O_4$, with deuteration on the aromatic H positions only, Cambridge Isotope Laboratories 98% purity, noted here d_4-BDC), ZnO (particle size < 5 μm, Sigma-Aldrich, 99.9% purity) and D_2O (Sigma-Aldrich, 99.9% purity).

^{17}O-labelled water (with ~ 40%, 70% or 90% ^{17}O enrichment) was purchased from CortecNet.

^{17}O-enriched H_2BDC was prepared either using a vibratory mixer mill as published elsewhere, or by scaling-up the procedure using a planetary ball mill.[58]

Mechanochemical syntheses

The Fritsch Pulverisette-23 (P23) vertical mixer mill was used in all reactions. BM syntheses were conducted in 10 mL inner-volume Perspex jars,[7] with two 10 mm diameter zirconia beads.

A typical mechanochemical synthesis was performed as follows. First, ZnO was introduced into a Perspex jar followed by H_2BDC (see **Table 2** for exact masses). Both powders were gently mixed with a spatula before adding the two zirconia beads. Finally, the appropriate amount of water was added. The jar was quickly closed and parafilm was added to cover the junction of top/bottom parts of the jar, to avoid any leaks as well as to increase air/water tightness. The system was then subjected to grinding for milling times ranging from 5 to 90 min in the P23 mixer mill operating at 30 or 50 Hz. The reactor was then opened and resulting compound was left to dry in air for several hours. The solid powder was then recovered by scraping the edges of the reactor and beads with a spatula. All samples were obtained as white powders.

Further details on the amounts of reagents and milling conditions used to isolate each of the four phases, in its non-labelled, ^{17}O-labelled or deuterated forms, are provided in **Table 2**. It is worth noting that for

the synthesis of ^{17}O-labelled compounds, amounts of reagents were reduced, in order to decrease the cost of the enrichment.

Table 2: Synthetic details for BM experiments of Zn-BDC compounds.

Code name	Formula	m_{ZnO} / mg	m_{H_2BDC} / mg	V_{H_2O} / µL	Milling parameters	
					Frequency / Hz	**Duration** / min
ZTA1	$Zn(BDC)(H_2O)_2$	129.9 *1 eq*	265.1 *1 eq*	115 *4 eq*	30	30
ZTA2a	$Zn_2(OH)_2(BDC)$	178.4 *2 eq*	182.1 *1 eq*	40 *2 eq*	50	20
ZTA2b	$Zn_2(OH)_2(BDC)$	197.8 *2 eq*	201.9 *1 eq*	350 *16 eq*	50	90
ZTA3	$Zn_3(OH)_4(BDC)$	262.1 *3 eq*	178.4 *1 eq*	310 *16 eq*	50	90
^{17}O-labelled compounds						
ZTA1-*BDC	$Zn(BDC)(H_2O)_2$	34.0 *1 eq*	71.0* *1 eq*	17 *2 eq*	50	5
ZTA2a-*BDC	$Zn_2(OH)_2(BDC)$	60.9 *2 eq*	63.6* *1 eq*	15 *2 eq*	50	12
ZTA2a-*OH	$Zn_2(OH)_2(BDC)$	178.4 *2 eq*	182.1 *1 eq*	40* *2 eq*	50	20
ZTA2b-*OH	$Zn_2(OH)_2(BDC)$	171.2 *2 eq*	174.7 *1 eq*	40* *2 eq*	50	90
ZTA3-*BDC	$Zn_3(OH)_4(BDC)$	121.1 *3 eq*	84.3* *1 eq*	50 *5 eq*	50	90
ZTA3-*OH	$Zn_3(OH)_4(BDC)$	81.4 *3 eq*	119.6 *1 eq*	50* *5 eq*	50	90
Deuterated compounds						
ZTA1-d_4BDC	$Zn(d_4BDC)(H_2O)_2$	125.0 *1 eq*	262.0[d] *1 eq*	315 *11.2 eq*	30	15
ZTA2a-d_4BDC	$Zn_2(OH)_2(d_4BDC)$	197.4 *2 eq*	207.5[d] *1 eq*	350 *16 eq*	50	90
ZTA2b-OD	$Zn_2(OD)_2(BDC)$	188.1 *2 eq*	192.8 *1 eq*	335[d] *16 eq*	50	90
ZTA3-d_4BDC	$Zn_3(OH)_4(d_4BDC)$	242.0 *3 eq*	168.7[d] *1 eq*	90 *5 eq*	50	90
ZTA3-OD	$Zn_3(OD)_4(BDC)$	250.7 *3 eq*	171.1 *1 eq*	350[d] *19 eq*	50	90

* is used for ^{17}O-labelled materials and [d] is used for deuterated materials, D_2O or d_4-BDC

"Routine" characterizations of the different phases

Powder XRD analyses were performed on an X'Pert MPD diffractometer using Cu Kα1 radiation (λ = 1.5406 Å) with the operation voltage and current maintained at 40 kV and 25 mA, respectively. Diffractograms were recorded between 2θ = 5° and 50° in Bragg-Brentano configuration, with a step size of 0.050°, and a time per step of 60 s.

Infrared (IR) spectra were recorded on a Perkin Elmer Spectrum 2 FT-IR spectrometer, using the ATR measurement mode (4000–400 cm^{-1} range, 4 repetitions).

***Operando* Raman spectroscopy & thermal analysis**

In this manuscript we use the term *operando* to insist on the fact that spectroscopic measurements were acquired during the milling (and without stopping the milling), as opposed to *in situ* analyses which can be performed on a medium when the milling is stopped for few seconds/minutes.[59]

The Raman measurements were performed with a WP 785 ER Raman spectrometer (Wasatch Photonics) using an IPS (Innovative Photonic Solutions) laser source (working at ~ 300 mW, wavelength of λ = 785 nm) and a contactless probe head. The positioning of the Raman probe was optimized such that the focus of the laser was localized at the inner jar wall. A laser exposure time of 5 s with 5 accumulations was chosen and spectrum collection was repeated every 30 s during the milling time. Raman spectra were collected across a range from 220 to 3120 cm^{-1}. The obtained Raman spectra were processed with the OriginPro 2021 program. Baseline correction (asymmetric least square smoothing) was first applied to each spectrum, then normalization of the signal of the Perspex jar (at 1728 cm^{-1}) was performed, prior to the subtraction of the signal of the vibrating empty jar.

Temperature measurements were carried out using an OPTRIS PI450i thermal imaging camera. The optical resolution of the device is 382 x 380 pixels. The temperature accuracy measured using this system is estimated to about ± 2°C. Four different temperatures were recorded every two seconds during the milling, focusing on three to four different areas, corresponding to the top, centre and bottom of the jar, and also to the "hot spot" at each time-point.

Cautionary remarks: The laser source used here is designed as a class IV during all procedures of operation, maintenance and service, meaning that safety measures must be taken accordingly. The use of laser specific safety goggles is required when operating this laser, as failure to wear appropriate eye protection may result in permanent eye damage. Caution must be taken to never look directly into the laser beam and make sure the laser direction points towards the wall. The power range for the laser is 0 – 580 mW. Measurements presented in this contribution were performed at ~ 300 mW in a dedicated isolated dark room with proper safety signs on the door, and operators have undergone specific security training before using this equipment.

Solid state NMR

^{1}H ssNMR

^{1}H ssNMR experiments were performed on a Varian VNMRS 600 MHz (14.1 T) NMR spectrometer, using a Varian 3.2 mm probe, tuned to ^{1}H (599.82 MHz). Spectra were recorded under magic angle spinning (MAS) conditions, with a spinning speed of 16 kHz, and under regulated air flow (0°C). A ^{1}H direct excitation pulse of 3.3 µs was used. Recycle delays used for the Zn-BDC compounds were 4 s, and 15 s for pure H_2BDC. Additional ^{1}H MAS NMR experiments were performed on a Bruker Avance NEO 850 MHz (20.0 T) NMR spectrometer, using a Bruker 1.3 mm probe, tuned to ^{1}H (850.23 MHz), with a spinning speed of 60 kHz. Adamantane was used as a secondary reference for setting ^{1}H chemical shifts (δ_{iso} = 1.8 ppm with respect to tetramethylsilane).

^{13}C ssNMR

^{13}C ssNMR experiments were performed on a VNMRS 600 MHz (14.1 T) NMR spectrometer, using a Varian 3.2 mm HX probe tuned to ^{1}H (599.82 MHz) and ^{13}C (150.81 MHz). All 1D ^{13}C NMR spectra consist of cross-polarization experiments (CP) under MAS conditions, with spinning frequencies from 4 to 15 kHz. A ^{1}H excitation pulse of 3.3 µs was used prior to a ramped spin-lock pulse of 5 ms contact time. Acquisition was performed under spinal-64 ^{1}H-decoupling (~ 75 kHz RF). Recycle delays used for the Zn-BDC compounds were 4 s, and 15 s for pure H_2BDC. ^{13}C chemical shifts were referenced to

adamantane, used as a secondary reference (high frequency peak at 38.5 ppm with respect to tetramethylsilane).

^{17}O ssNMR

^{17}O ssNMR experiments were first performed on all samples on a Varian VNMRS 600 MHz (14.1 T) NMR spectrometer, using either Varian 3.2 mm HX or HXY probes, or a Phoenix 3.2 mm probe, tuned to ^{1}H (599.82 MHz) and ^{17}O (81.31 MHz). Spectra were recorded under MAS conditions under regulated air flow (0°C), with spinning speeds ranging from 16 to 20 kHz, depending on the sample. Additional ^{17}O MAS NMR experiments were performed at lower field on a VNMRS 400 MHz (9.4 T) NMR spectrometer, using a Varian 3.2 mm HXY probe tuned to ^{1}H (399.92 MHz) and ^{17}O (54.21 MHz). Moreover, higher field ^{17}O NMR analyses were performed first on a Bruker Avance NEO 850 MHz (20.0 T) NMR spectrometer, using Bruker 1.3 or 4 mm probes, tuned to ^{1}H (850.23 MHz) and ^{17}O (115.26 MHz) and then on a Bruker Avance III HD 800 MHz (18.8 T) NMR spectrometer using a 3.2 mm Low-E probe spinning at 16 kHz ($\nu_L(^1H)$ = 800.12 MHz and $\nu_L(^{17}O)$ = 108.47 MHz) in order to perform multi-magnetic field data fitting (see ESI **Figure S13 – S16**). A double frequency sweep (DFS) excitation scheme was used consisting of a 1 ms pulse with a sweep between 1 MHz and 50 kHz,[60]–[62] for ^{17}O-signal enhancement when possible, prior to the excitation pulse, and spinal-64 ^{1}H-decoupling was applied during acquisition. The acquisition parameters used for each sample can be found in **Table 3**. The D-HMQC (Dipolar-Heteronuclear Multiple-Quantum Coherence) sequence used a $SR4^2_1$ recoupling scheme on the ^{1}H channel with a radio frequency field of twice the spinning speed, the detection is performed on the ^{17}O channel.[63] ^{17}O chemical shifts were referenced externally to D_2O at −2.7 ppm (or tap water at 0.0 ppm).

Table 3: Main acquisition parameters for ^{17}O NMR experiments.

Sample	Field / T	$Ø_{rotor}$ / mm	Expt	ν_{rot} / kHz	R delay / s	NS (/ #t1)	ν_{RF} / kHz	Pulses / µs	Dec {^{1}H} / kHz
ZTA1-*BDC	14.1	3.2	DFS-One pulse	18	2	1024	~40	2	75
	20.0	3.2	DFS-One pulse	14.286	4	256	10	8.33	60
ZTA2a-*BDC	9.4	3.2	DFS-One pulse	18	1	20480	~40	2	50
	14.1	3.2	DFS-One pulse	18	1	6144	~40	2	75
	18.8	3.2	MQMAS	16	5	768 / 22	~16	3 / 1 / 5	62.5
	20.0	4	DFS-One pulse	14.286	1	4096	10	8.33	60
ZTA2a-*OH	9.4	3.2	DFS-One pulse	18	2	512	~40	2	50
	14.1	3.2	DFS-One pulse	18	2	3072	~40	2	75
	20.0	4	DFS-One pulse	14.286	2	256	10	8.33	60
ZTA2b-*OH	9.4	3.2	DFS-One pulse	18	4	3072	~40	2	50
	14.1	3.2	DFS-One pulse	18	4	1024	~40	2	75
	20.0	4	DFS-One pulse	14.286	4	512	10	8.33	60
ZTA3-*BDC	9.4	3.2	DFS-One pulse	18	2	6144	~40	2	50
	14.1	3.2	DFS-One pulse	18	2	12288	~40	2	75
	18.8	3.2	MQMAS	16	5	768 / 32	~16	3 / 1 / 5	62.5
	20.0	4	DFS-One pulse	14.286	2	1024	10	8.33	60
		1.3	(DFS) D-HMQC	60	4	9216 / 24	20	4.167 / 8.33	75
ZTA3-*OH	9.4	3.2	DFS-One pulse	18	4	10240	~40	2	50
	14.1	3.2	DFS-One pulse	18	4	1024	~40	2	75
	18.8	3.2	MQMAS	16	5	480 / 32	~16	3 / 1 / 5	62.5
	20.0	4	DFS-One pulse	14.286	4	256	10	8.33	60
		1.3	(DFS) D-HMQC	60	2	1536 / 23	20	4.167 / 8.33	75

The NMR parameters were obtained by fitting the spectra using DMfit.[64]

NMR conventions

In this article the "Herzfeld-Berger" convention is used to describe the magnitude of the chemical shift anisotropy (CSA) arising from the magnetic shielding interaction.[65] The isotropic chemical shift (δ_{iso}), span (Ω), and skew (κ) are given as follows:

(1) $$\delta_{iso} = \frac{(\delta_{11} + \delta_{22} + \delta_{33})}{3}$$

(2) $$\Omega \approx \delta_{11} - \delta_{33} \ (\Omega \geq 0)$$

(3) $$\kappa = \frac{3(\delta_{22} - \delta_{iso})}{\Omega} \ (-1 \leq \kappa \leq +1)$$

The principal components of the chemical shift tensor are ordered as follows: $\delta_{11} \geq \delta_{22} \geq \delta_{33}$.

The quadrupolar interaction is described by two parameters, the quadrupolar coupling constant (C_Q) and the asymmetry parameter (η_Q).

(4) $$C_Q = \frac{eQV_{33}}{h}$$

(5) $$\eta_Q = \frac{V_{11} - V_{22}}{V_{33}}$$

Here, V_{11}, V_{22}, V_{33} are the principal components of the traceless electric field gradient (EFG) tensor, with $|V_{33}| \geq |V_{22}| \geq |V_{11}|$, e is the fundamental electronic charge, Q the nuclear quadrupole moment and h the Planck's constant.

GIPAW-DFT calculations

The unit cell parameters were set to the X-ray diffraction parameters and kept fixed during geometry optimizations to ensure consistency between experimental and optimized structures. Missing protons (in CCDC PUCYAO and PEKGAO structures) were initially positioned to be consistent with the expected structure of the system, and successively only protons and then all atomic positions were relaxed with the VASP (Vienna Ab-initio Simulation Package) code [66] based on the Kohn-Sham Density Functional Theory (DFT) and using a plane-wave pseudopotential approach. For the two structures mentioned above, several initial OH proton positions were tested. The NMR parameters were then calculated within Kohn-Sham DFT using the QUANTUM-ESPRESSO code[67], [68] keeping the atomic positions equal to the values previously calculated with VASP. The PBE generalized gradient approximation[69] was used and the valence electrons were described by norm conserving pseudopotentials[70] in the Kleinman Bylander form[71]. The shielding tensor was computed using the Gauge Including Projector Augmented Wave (GIPAW) approach,[72] which enables the reproduction of the results of a fully converged all electron calculation.[73] The isotropic chemical shift δ_{iso} is defined as $\delta_{iso} = -[\sigma - \sigma^{ref}]$, where σ is the isotropic shielding and σ^{ref} is the isotropic shielding of the same nucleus in a reference system. For ^{1}H, ^{13}C and ^{17}O, previously used referencing was adopted using glycine,[74] calcite [75] and a series of silicates[56] respectively. Diagonalization of the symmetrical part of the calculated tensor then provides its principal components σ_{11}, σ_{22}, σ_{33} from which the chemical

shift components δ_{11}, $\delta_{22,}$ δ_{33} can be calculated. The principal components V_{xx}, V_{yy}, and V_{zz} of the electric field gradient (EFG) tensor are obtained by diagonalization of the tensor. The quadrupolar interaction can then be characterized by the quadrupolar coupling constant C_Q and the asymmetry parameter η_Q, which are defined previously. The experimental value of the quadrupole moment of ^{17}O (Q = –25 × 10^{-30} m^2) was used to calculate C_Q.[76]

Results & Discussion

Given the rich variety of structures involving Zn^{2+} and BDC ligands, in terms of Zn/BDC ratios, H_2O or OH species linked to the Zn^{2+}, and also carboxylate coordination modes, we decided to investigate the formation of these compounds using mechanochemistry, a synthetic method which had not yet been tested in a systematic way for these phases. The general idea was to see if conditions allowing each of these phases to be isolated in a pure form and high yield could be achieved using mechanochemistry. Coupled with the use of ^{17}O-enriched precursors, this approach would allow all the different forms of Zn-BDC to be analysed with an unprecedented level of detail, and to provide useful information to the debate related to the structures of these materials.

Formation and isolation of zinc (hydroxyl-) terephthalate coordination complexes

Observation of several intermediate phases

The three reagents, namely H_2BDC, ZnO and H_2O, were introduced in a Perspex milling jar to enable the monitoring of different vibration bands by Raman spectroscopy. An illustrative example of the formation of various Zn-BDC phases in a one pot mechanochemistry synthesis is shown in **Figure 1**, for a $ZnO/H_2BDC/H_2O$ stoichiometry of 2/1/16. In **Figure 1a**, the evolution of the Raman signals during the milling for two selected regions of the spectra are presented after data processing (see Experimental section for more information). It is worth noting that water plays multiple roles in this system: i/ it is directly involved in the reaction by forming complexes with the Zn^{2+} cations, and in some cases leads to the formation of coordinated hydroxyls, ii/ it plays the role of a *liquid assisted grinding* (LAG) agent, allowing a better mixing of the solid reagents and thus a better efficiency of the milling process,[77], [78] iii/ it guarantees the formation of a paste-like materials during the milling which will be homogeneously spread over the inner surfaces of the milling jar. The latter point is of great importance for the *operando* Raman measurements, justifying the use of an excess amount of water in this particular example ($\geq$ 16 equivalents).

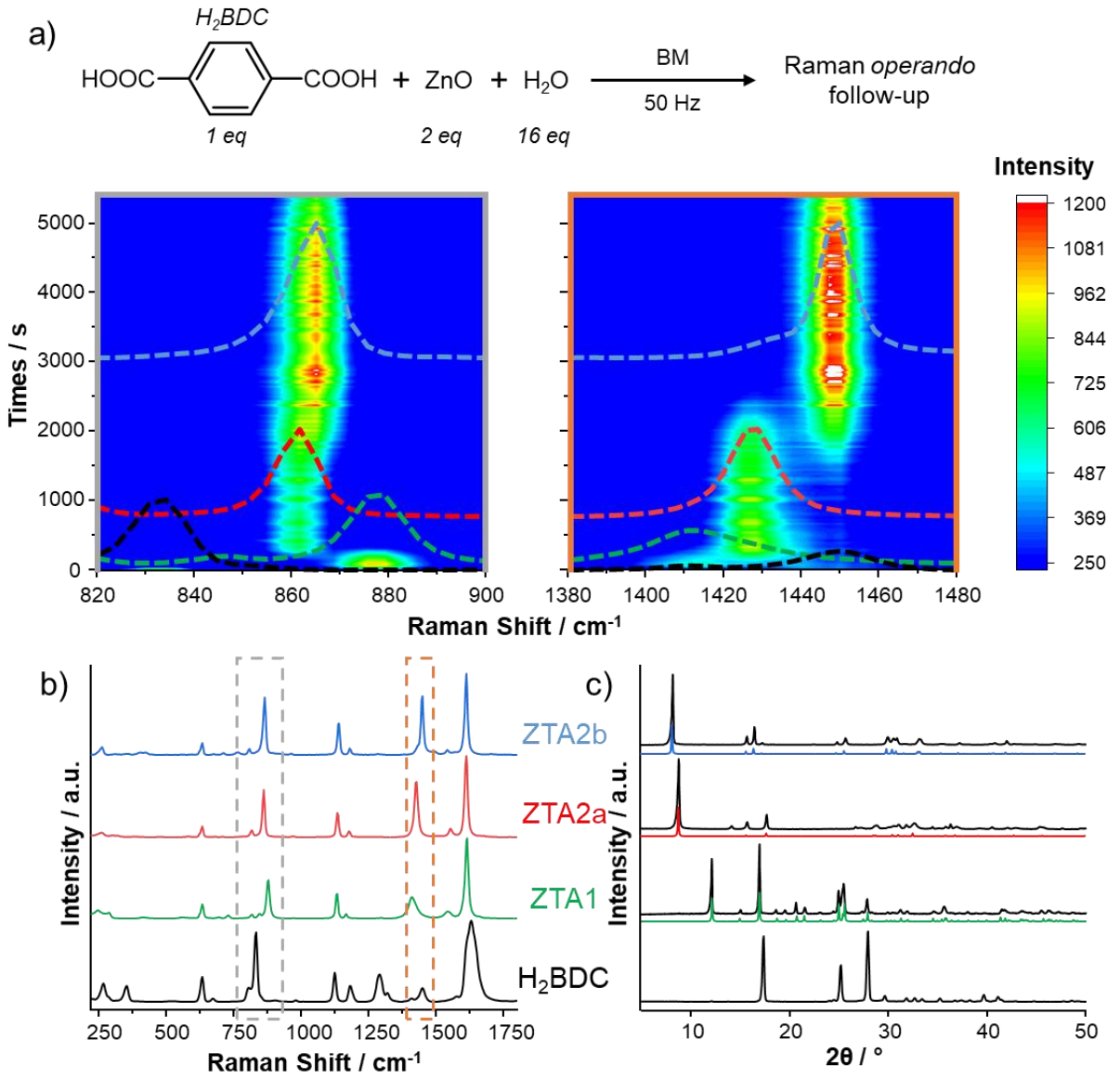

Figure 1: a) Top: Starting compounds used for the operando experiment with their respective equivalents and milling conditions. Bottom: Time-resolved operando Raman spectra of two selected areas (grey and orange - see b): 820-900 cm^{-1} range on the left, and 1380-1480 cm^{-1} range on the right; 2D plots have been overlapped with spectra from b .b) Experimental ex situ Raman spectra of ***H$_2$BDC*** *(in black),* ***ZTA1*** *(in green),* ***ZTA2a*** *(in red) and* ***ZTA2b*** *(in blue), when isolated under the milling conditions reported in* ***Table 2.*** *c) Experimental ex situ pXRD diffractograms of the corresponding "pure" compounds, when isolated under the milling conditions reported in* ***Table 2*** *(in black), and comparisons with the simulated pXRD data for these Zn-BDC phases (coloured lines; pXRD simulated from available CIFs in the CCDC database, as reported in* ***Table 1****).*

The system undergoes several structural transformations during the milling process, as illustrated by the shifts of specific vibration modes in the time-resolved experiment (**Figure 1a**). Between 800 and 900 cm^{-1} (**Figure 1b** grey box), we focus on the aromatic breathing region.[79] The signal from the starting H_2BDC molecule quickly shifts from 832 to 878 cm^{-1}, and after ~ 8 min of

milling, it evolves to 862 cm^{-1}, and finally moves to 865 cm^{-1} in the final compound. Accordingly, corresponding modifications of ν_s(CO) band can also be easily followed between 1380 and 1480 cm^{-1}.

The products successively formed were identified as **ZTA1**, **ZTA2a** and **ZTA2b**. Their Raman spectra as well as pXRD patterns are presented in **Figure 1b** and **c**, in green, red and blue, respectively. No formation of **ZTA3** occurred when using an initial Zn/BDC molar ratio of 2/1 in the milling.

Kinetic study of the transformations

In view of describing further the reactions occurring during the milling, the kinetic evolution of the reaction medium established by Raman spectroscopy (as determined by integration of the previously mentionned vibration modes between 800 and 900 cm^{-1}, for example), was complemented with the thermal imaging of the milling jar (**Figure 2**). Simultaneous recording of temperatures at three different areas of the jar (referred to as top, centre and bottom) led to the plots displayed on **Figure 2b**. The insert (dashed grey area in **Figure 2a**) presents the first 500 s of the experiment, corresponding to the transformation of H_2BDC into **ZTA1** (from 832 to 878 cm^{-1}), which has a 1/1 Zn/BDC molar ratio.[39] This reaction is then followed by the introduction of an additional Zn^{2+} centre in the structure and the deprotonation of two water molecules, to form, after less than 8 minutes (< 480 s) of milling, the **ZTA2a** phase (with characteristic bands at 862 cm^{-1} and 1424 cm^{-1} in the two aforementioned regions) which has a Zn/BDC ratio of 2/1 (red curve). The reaction is probably exothermic, as shown by the increase of the temperature up to ~ 40°C (grey curve in **Figure 2b**). The final transformation observed on **Figure 1a** corresponds to the structural modification of **ZTA2a** to form the polymorph **ZTA2b** (865 cm^{-1} and 1424 cm^{-1}) with a second increase of the temperature up to ~ 47°C (for the centre temperature).

The fact that the apparent proportion of **ZTA2a** is not null at the end of the reaction on **Figure 2a** (despite the fact that its resonances have disappeared from the Raman data) can be explained by the way in which these kinetic plots were only "coarsely" fitted here, by using simple Gaussian signals centred at the different maximum frequencies of the intermediates, with intensities which were left to freely evolve at each timepoint. This created ambiguities in the fitted intensities due to the closely

overlapping signals of **ZTA2a** and **ZTA2b.** More accurate kinetic plots could be obtained by fitting the 1380 -1480 cm^{-1} region from 1000 to 5400 s (see ESI, **Figure S1**), which shows the decrease of **ZTA2a** close to 0 % at the end of the reaction (as confirmed by pXRD analyses). Because the purpose of this manuscript was not to establish a full kinetic model of the formation of these Zn-BDC phases, no attempt was made to further refine or analyse this operando Raman data. Yet, it is worth noting that this example illustrates the importance of having access to different regions of the Raman spectra in order to evaluate the quality of such kinetic fits. Other possibilities along this line (*e.g.* with deuterated precursors) will be discussed at the end of this article.

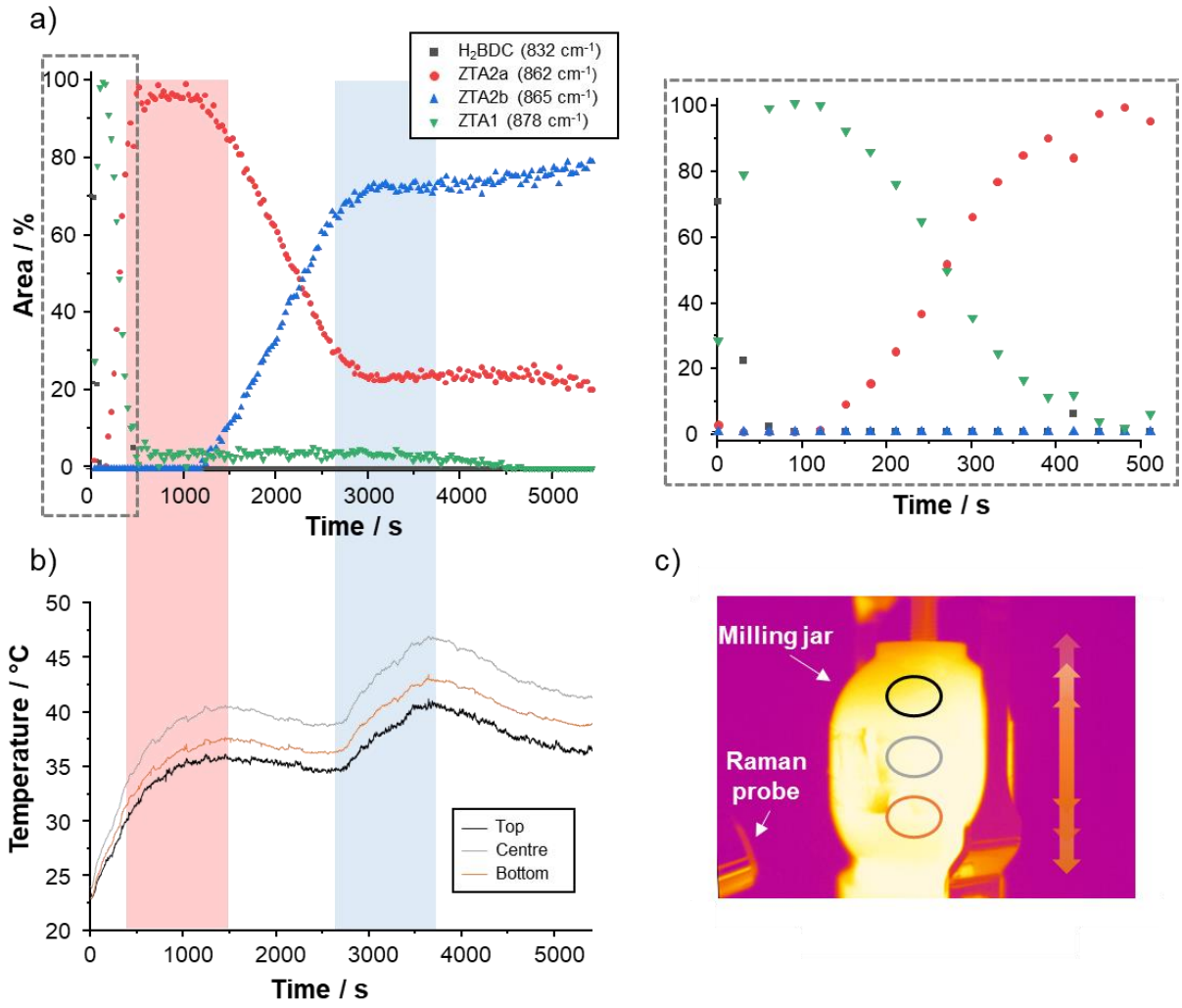

*Figure 2: a) Reaction profiles corresponding to signals highlighted in **Figure 1b**. The insert on the right-hand side corresponds to a zoom of the first 500 s on of the time resolved Raman experiment. b) Temperature profiles of three different areas of the jar. c) Picture obtained with the thermal imaging camera of the milling jar, highlighting the three measurement zones. The shaking direction is emphasized by the orange arrows.*

In the frame of this work, the clear identification of each transformation thanks to the *operando* set-up involving the combined use of the Raman instrument and the thermal camera allowed each of these structures to be isolated as pure phase for further *ex situ* structural analyses (using the optimized reaction conditions reported in **Table 2**). Similarly to **ZTA1**, **ZTA2a** and **ZTA2b**, the formation of **ZTA3** could also be followed in the same fashion by *operando* Raman spectroscopy, when starting from a 3/1 ratio between the ZnO and H_2BDC precursors. Hence, by choosing the adequate stoichiometry and by stopping the milling at carefully selected times, the different Zn-BDC phases could be isolated pure, without them changing with time (see ESI **Figure S2**). It then became conceivable to refine their structures, especially the protons positions, and to gain more insights in the terephthalate binding modes.

Refinement of the Zn-BDC structures using an "NMR-crystallography" approach

When the limits of XRD methods are reached, for example for phases which cannot be isolated as single crystals, in which some atoms cannot be positioned (*e.g.* protons), or which contain defects, ssNMR methods can be particularly useful when used in conjuction with computational modeling, in order to gain precise information on the crystallographic structures. Such an approach, referred to as "NMR-crystallography",[80], [81] implies that the structures of interest possess NMR-active isotopes which can be readily analysed by high-resolution NMR.

In the case of Zn-BDC structures, the vicinity of the Zn^{2+} cations, and more specifically the precise coordination modes of the BDC and hydroxyl ligands to Zn^{2+} are of great importance. From an NMR perspective, all atoms present in these phases have at least one NMR-active isotope which can be studied by NMR, making them potentially attractive targets of analysis: ^{1}H (I = 1/2, 100% natural abundance), ^{13}C (I = 1/2, 1.07% natural abundance), ^{17}O (I = 5/2, 0.04% natural abundance) and ^{67}Zn (I = 5/2, 4.11% natural abundance). Even though ^{67}Zn NMR has recently shown promising results for providing a detailed description of zinc local environments, it is still considered as very challenging,[82] because of the quadrupolar nature of zinc-67 (which can lead to very broad lines),[83] and its poor receptivity (low natural abundance and very low resonance frequency ($\nu_L(^{67}Zn) < 10\% \nu_L(^{1}H)$).[82], [84] In the present work, we thus set our focus on the other 3 nuclei (^{13}C, ^{17}O and ^{1}H) to reach a more detailed

description of the binding mode of the dicarboxylate ligands and for positioning the H-atoms of the hydroxyls within the structures.

^{13}C NMR analyses of carboxylate binding modes in Zn-BDC structures

As briefly explained earlier (*vide supra*), IR spectroscopy has been used for decades as a first approach for proposing binding modes of carboxylates to various metal ions. The difference in wavenumbers between the antisymmetric and symmetric stretching modes, defined by the parameter Δ (= $\nu_{as}(COO^-)$-$\nu_s(COO^-)$), has been shown to change depending on the binding mode of carboxylates, allowing, as a first approximation, the following tendency to be derived upon coordination to divalent metal ions: $\Delta(Chelating) < \Delta(Bridging) < \Delta(Ionic) < \Delta(Monodentate)$ (see **Figure 3a**).[46] However, this method can be quite ambiguous as Δ can be affected by other parameters, depending on the types of ligands involved, and how they interact with each other within the structures. Moreover, it relies on the clear attribution of the vibration modes ($\nu_{as}(COO^-)$ and $\nu_s(COO^-)$) which remains uncertain in numerous cases, due to overlapping vibration bands on the IR spectra (see ESI **Figure S3**). For example, when looking at the FTIR spectrum of **ZTA2a**, the Δ = 210 cm^{-1} splitting is significantly higher than expected for bridging ligands. Indeed, the other phases with bridging ligands, namely **ZTA2b** and **ZTA3**, display values at Δ = 171 and 180 cm^{-1} respectively. Moreover, the monodentate bound ligand in **ZTA1** shows a splitting of Δ = 192 cm^{-1}. Overall, this tends to show the limitations of IR spectroscopy in providing direct information on the terephthalate binding modes, but may also suggests that **ZTA2a** actually exhibits more complex binding modes than suggested by the X-ray diffraction data.

Here, we decided to perform ^{13}C ssNMR analysis in order to obtain more information on the binding mode of the carboxylates. The ^{13}C ssNMR spectra of the 4 samples obtained by mechanochemistry are presented on **Figure 3b** (see ESI **Figure S4** for H_2BDC data). Spectra were recorded with different spinning speeds, such as to focus on the isotropic chemical shifts (**Figure 3b**, left), or to derive the chemical shift anisotropy (CSA) parameters (**Figure 3b**, right).

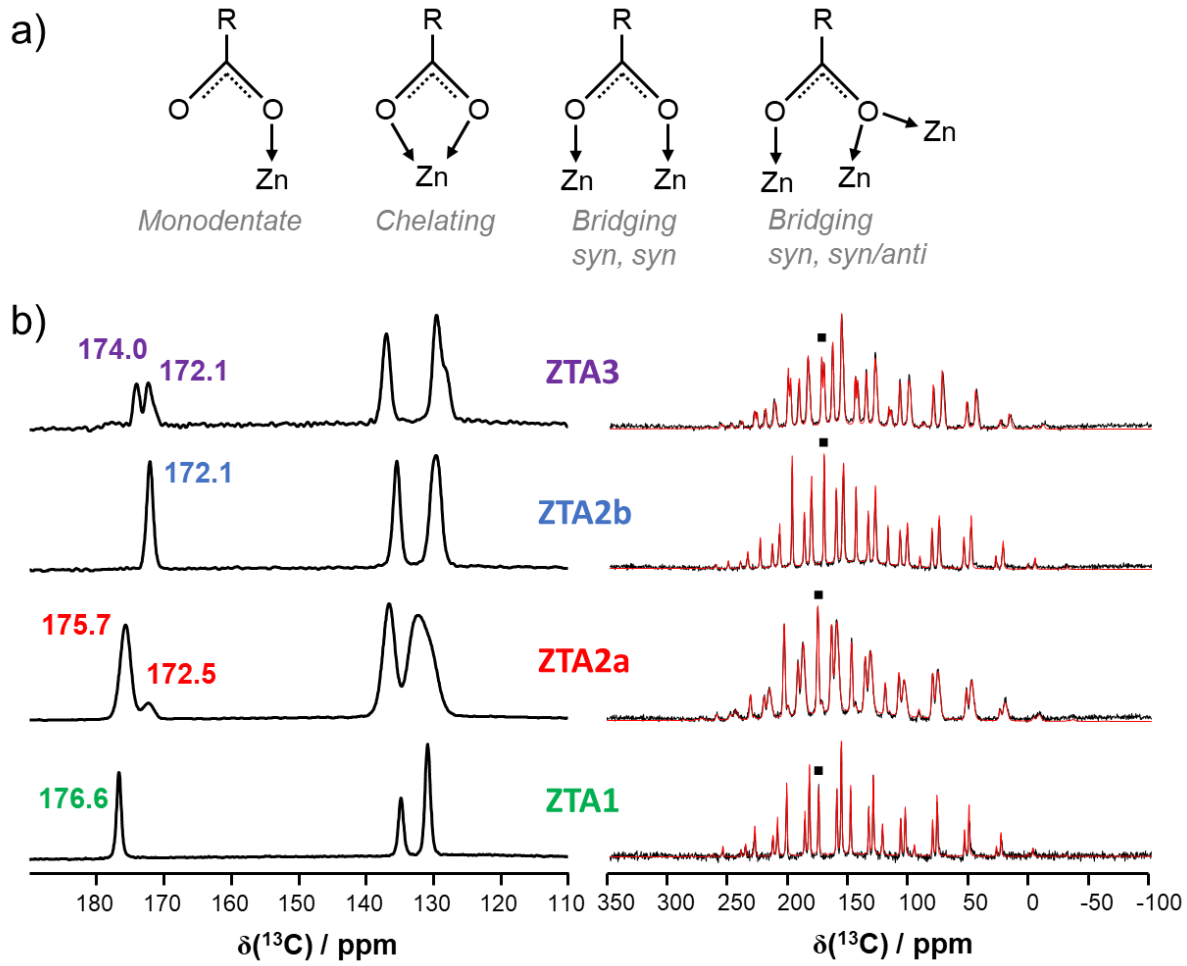

Figure 3: a) Different possible binding modes of carboxylate ligands to Zn^{2+} ions. b) Left: ^{13}C CP MAS NMR spectra recorded at 14.1 T with a spinning speed of 15 kHz under regulated temperature 0 °C. Right: ^{13}C CP MAS NMR spectra recorded at 14.1 T with a spinning speed of 4.0 or 4.2 kHz under regulated temperature 0 °C. ▪ indicates the isotropic shifts. The parameters used for fitting the spectra (in red) are gathered in ***Table 4****.*

Table 4: ^{13}C NMR parameters extracted from fitting spectra recorded at multiple spinning speeds, and calculated ones using DFT from optimized structural models of the phases.

	Experimental			Calculated (GIPAW-DFT)[a]			
				H-Relaxed	*Fully optimized structures*		
Compound	δ_{iso} / ppm	**Ω** / ppm	**κ**	δ_{iso} / ppm	δ_{iso} / ppm	**Ω** / ppm	**κ**
ZTA3	172.1 ± 0.3	136.9 ± 0.4	0.05 ± 0.01	167.6	172.4	130.7	0.15
	174.0 ± 0.1	139.9 ± 2.4	0.13 ± 0.01	168.0	175.6	132.3	0.31
ZTA2b	172.1 ± 0.1	137.4 ± 0.2	0.22 ± 0.01	168.0	173.4	136.2	0.15
ZTA2a	172.5 ± 0.2	140.0 ± 8.2	0.34 ± 0.15				
	175.7 ± 0.1	137.5 ± 0.4	0.20 ± 0.01	199.4	177.6	141.7	0.23
ZTA1	176.6 ± 0.1	154.7 ± 6.3	0.03 ± 0.02	176.5	181.8	146.4	0.35

[a]A systematic study of ^{13}C chemical shifts was performed in 2009 on 14 molecules (aromatics and carbohydrates) whose crystal structures have been precisely determined by neutron diffraction. This study showed that the GIPAW ^{13}C predictions are more accurate than a cluster approach with an error on the isotropic shift of ~1 ppm.[85]

Based on the reported crystal structures (see **Table 1**), two main binding modes were expected for the Zn-BDC compounds of interest: monodentate and bridging. For **ZTA1**, BDC ligands exhibit a monodentate configuration, and only one crystallographically inequivalent carboxylate carbon is present in the structure. For this phase, a single resonance was observed in the carboxylate region of the ^{13}C ssNMR spectrum (**Figure 3b**), with $\delta_{iso}(^{13}COO)$ = 176.6 ppm. On the other hand, **ZTA2b** and **ZTA3** structures have different types of bridging terephthalate ligands based on the reported X-ray diffraction data. While the former clearly exhibits a single carboxylate environment ($\delta_{iso}(^{13}COO)$ = 172.1 ppm), as expected from the crystal structure, the latter shows two main carboxylate resonances centred at 174.0 and 172.1 ppm (with an additional and yet unexplained shoulder in the low frequency resonance). Finally, for the **ZTA2a** phase, while only one carbon signal was expected from the crystallographic structure, two carboxylate resonances were observed, centred at 175.7 and 172.5 ppm, present in a ~ 5/1 ratio. The weaker low-frequency resonance was systematically observed for this phase (for different synthetic batches), and with the same approximate ratio. Although its ^{13}C chemical shift is relatively close to the one of the H_2BDC precursor (173.5 *vs.* 172.5 ppm), no traces of residual H_2BDC could be detected by IR spectroscopy in the C=O stretching region, and no acidic proton signal was observed by

^{1}H ssNMR, meaning that this small signal cannot arise from the presence of residual H_2BDC (see ESI **Figure S5** & **S6**). Moreover, given that no diffraction peaks ascribable to known impurities could be detected on the X-ray diffraction pattern of **ZTA2a** (see **Figure 1c** and ESI **Figure S2**), the weak resonance must correspond to systematic defects in the crystal structure, which could not be resolved nor identified by X-ray diffraction.[86]

In the literature, few articles report ^{13}C ssNMR data for zinc-carboxylates, and more specifically Zn-BDC phases.[36], [48]–[50] In all cases, $\delta_{iso}(^{13}COO)$ was found to vary between 171.8 to 177.7 ppm. Moreover, when comparing the reported $\delta_{iso}(^{13}C)$ values of bridging carboxylates versus monodentate ones, a trend can be extracted. Indeed, the $\delta_{iso}(^{13}COO)$ values of monodentate ligands are nearly systematically more deshielded than the $\delta_{iso}(^{13}COO)$ of bridging ones. For example, Yuan *et al.* reported values of $\delta_{iso}(^{13}COO)$ = 176.7 and 177.3 ppm for two Zn-BDC phases exhibiting monodentate binding modes (the first phase was actually the same as **ZTA1**, while the second one was Zn(BDC)(H_2O)), and for a Zn-BDC·DMF MOF with bridging terephthalates, they reported $\delta_{iso}(^{13}COO)$ = 172.7 ppm.[49] Similarly, Julien *et al.* showed that the Zn(H_2O)$_2$(2,5-dihydroxyterephthalate) structure, which displays a monodentate configuration, exhibits a ^{13}C resonance at $\delta_{iso}(^{13}COO)$ = 176.0 ppm, while MOF-74, with bridging 2,5-dihydroxyterephthalate ligands, shows signals at $\delta_{iso}(^{13}COO)$ = 173.2 and 173.9 ppm (for compounds obtained by LAG using either H_2O or DMF, respectively).[50] Habib *et al.* also studied two Zn-dicarboxylate complexes, [$Zn_2(\mu_2$-BDC)$_2(\mu_4$-btre)] and [$Zn_2(\mu_3$-ip)$_2(\mu_2$-btre)(H_2O)$_2$]·2H_2O (with btre = 1,2-bis(1,2,4- triazol-4-yl)ethane, ip = benzene-1,3-dicarboxylate). Each structure exhibits two distinct $\delta_{iso}(^{13}COO)$ by ^{13}C ssNMR corresponding to two monodentate binding modes ($\delta_{iso}(^{13}COO)$ = 174.4 and 173.3 ppm) for the first one, while the second complex has a bridging and a monodentate ligands ($\delta_{iso}(^{13}COO)$ = 174.6 and 176.7 ppm).[48] Based on this literature survey, which shows that the $\delta_{iso}(^{13}COO)$ values for monodentate binding modes are deshielded compared to bidentate ones, it was found that the isotropic ^{13}C shifts of the carboxylates in **ZTA1**, **ZTA2b** and **ZTA3** also fall very well in this trend. In contrast, for **ZTA2a**, there seem to be discrepancies with what one would have expected from the reported crystal structure, not only in the number of ^{13}C resonances (due to the additional small peak – *vide supra*), but also in the ^{13}C isotropic shift of the main resonance, which is rather high for a

"bridging mode". Hence, overall, this points once again to the issues related to the X-ray data available for this phase.

To go further in the study of these, we conducted various DFT optimizations of the different structures studied here. Starting from the reported crystal structures, H atoms were positioned (when missing). Then, keeping cell parameters constant, geometry optimizations were performed, by optimizing either H positions only, or all atomic positions. The H-relaxed structures did not lead to satisfactory results after computation of NMR parameters, except for **ZTA1** (as illustrated for $\delta_{iso}(^{13}COO)$ in **Table 4**). A more complete geometry optimization was thus needed to refine the various crystal data. Moreover, for some of the structures, it was necessary to test various initial H orientations for the hydroxyls before geometry optimization, in order to converge towards a model which matches best the experimental data; this will be further detailed for **ZTA3** later in this article. In all cases, after these additional geometry optimization steps, the GIPAW calculated NMR parameters for ^{13}C were found to be in good agreement with the experimentally extracted values. Notably, $\delta_{iso}(^{13}COO)_{calc}$ of the monodentate **ZTA1** ligand was the most deshielded of the series, with a calculated ^{13}C chemical shift at 181.8 ppm, while $\delta_{iso}(^{13}COO)_{calc}$ from bridging ligands were ~ 6-10 ppm lower in frequency. Moreover, the calculated chemical shift anisotropy (CSA) parameters after full geometry optimization were also found to be in relatively good agreement with the experimental values, as further discussed below. These DFT-optimized structures can thus be considered as more reliable structural models of the four Zn-BDC phases studied here (see ESI **Figure S7**).

Following this, the structures after full relaxation of atom positions were analysed in detail, and relationships between calculated ^{13}C NMR parameters and local environments of the carboxylates (in the geometry-optimized structures) were looked into (see ESI **Figure S8**). Significant structural modifications were observed upon full geometry optimization of some of the phases. For example, the **ZTA3** crystallographic structure was found to undergo various changes, the major one being the modification of one zinc coordination from a 5-fold O-coordination environment (Zn2 in **Table 1**) to a 4-fold one. In the case of **ZTA2a**, significant variations in the carboxylate binding modes were observed during the relaxation of all atom positions, which can explain the ~20 ppm decrease in the $\delta_{iso}(^{13}COO)_{calc}$

value between H-relaxed and fully relaxed models (see **Table 4**). Still for this phase, the calculated ^{13}C NMR parameters were found to be in good agreement with those of the most intense ^{13}C resonance (*i.e.* $\delta_{iso}(^{13}COO)_{exp}$ = 176.4 ppm *vs.* $\delta_{iso}(^{13}COO)_{calc}$ = 175.7 ppm), again with a relatively high chemical shift compared to what one may have expected for bridging carboxylates. Yet, when looking more closely at the local environment of the carboxylate after full geometry optimization, the coordination mode was actually found to be closer to a bridging *syn,syn/anti* configuration (see **Figure 3a**) than monodentate or bridging *syn,syn* ones. In such configuration, one of the $d_{Zn\cdots O}$ distances was found to be shorter (in the range of $d_{Zn\cdots O}$ for *syn,syn* bridging modes, *i.e.* ~ 2.0 Å) than the two others (which were measured between 2.2 and 2.3 Å). This may be one of the reasons to the higher ^{13}C shift of this phase, compared to bridging modes involving only shorter Zn⋯O bonds.

In order go even further in trying to relate ^{13}C NMR parameters to structural/geometric information about carboxylate bindings, the calculated data collected from the numerous geometry optimizations on Zn-BDC phases (especially the **ZTA3** structure) were compiled. The most obvious trend we found was between the $\delta_{iso}(^{13}COO)_{calc}$ and the longest C-O distance of the carboxylate, $(d_{C-O})_l$: the highest chemical shifts are clearly related to structures with the longest C-O distances $(d_{C-O})_l$ (see ESI **Figure S8**). *A contrario*, no unambiguous relationship relating $\delta_{iso}(^{13}COO)$ and the type of carboxylate coordination could be extracted, showing that this parameter depends on several factors.

As ^{13}C CSA parameters can also be used to describe the local environment of carbon atoms, these were extracted from the experimental ^{13}C NMR spectra recorded at two different spinning speeds (**Table 4**). The most noticeable difference between compounds was in the CSA span (Ω), which was found to be experimentally higher by approximately 15 – 20 ppm for **ZTA1** (monodentate binding), than for the carboxylates of the three other compounds (155 ppm *vs.* 135 – 140 ppm respectively) (see ESI **Figure S9** and **Table S1**). DFT-calculated values of spans also followed the observed trend, with the highest value for **ZTA1**, with however the calculated span of **ZTA2a** now only about 5 ppm lower than the one calculated for **ZTA1**. Using the data library obtained by optimizing the Zn-BDC structures and also different structural models of **ZTA3**, attempts were made to relate the various CSA parameters stemming from the calculations to carboxylate binding modes. Here, a general trend was also observed

between the longest C-O distance and Ω_{calc} (see ESI **Figure S10**), but no direct relationship with the carboxylate coordination.

Overall, although hints about carboxylate binding modes could be derived from ^{13}C ssNMR spectra, we then considered analysing local environments of oxygen atoms, because they are directly coordinated to the Zn^{2+} ions in the Zn-BDC structures, and may help gain insights into the various binding modes.

^{17}O NMR analyses of carboxylate and hydroxyl binding modes in Zn-BDC structures

With the aim of directly probing the binding modes of the terephthalate ligands by using ^{17}O ssNMR, ^{17}O-labelled terephthalic acid was used as a starting material to prepare Zn-BDC phases enriched on the carboxylate groups. Concerning the bridging hydroxyls, a direct enrichment during the mechanochemical synthesis of the Zn-BDC phases was envisaged by using ^{17}O-enriched water as a starting reactant (instead of normal water).

Both labelling strategies were tested for each compound (**ZTA1, 2a, 2b** and **3**), in order to isolate Zn-BDC phases selectively enriched on the carboxylates or on the hydroxyls/water, and then perform high-resolution NMR spectroscopy. All samples could be prepared by mechanochemistry, with selective enrichment on the carboxylate part (phases noted **ZTA-*BDC**) or the hydroxyl/water part (phases noted **ZTA-*OH**), with the exception of **ZTA2b**, for which the carboxylate-enriched phase (**ZTA2b-*BDC**) could not be obtained with a sufficient purity to be analysed by ^{17}O ssNMR. In total, 6 different enriched samples were thus isolated with good purity, using the BM synthetic procedure developed above thanks to the *operando* Raman set-up. In all cases, preliminary evidence of the success of the enrichment could be assess by FTIR with the slight shifts of vibration modes such as $\nu_{as}(COO^-)$ and $\nu_s(COO^-)$ (see ESI **Figure S3c**). The corresponding 1D ^{17}O MAS NMR spectra are presented in **Figure 4**, which could all be recorded with good sensitivity in just a few hours.

Because oxygen-17 is a quadrupolar nucleus, the NMR resonances recorded on the 1D spectra show characteristic second order quadrupolar lineshapes. In order to extract the ^{17}O NMR parameters

associated with each oxygen environment (δ_{iso}, C_Q and η_Q), spectra were fitted at multiple fields (see ESI **Figure S13 – S16**), since the second-order quadrupolar broadening decreases as the magnetic field increases. Moreover, additional 2D high-resolution MQMAS (multiple-quantum MAS) experiments were also recorded for some of the phases, allowing the fits to be further refined (see ESI **Figure S11** and **S12**).

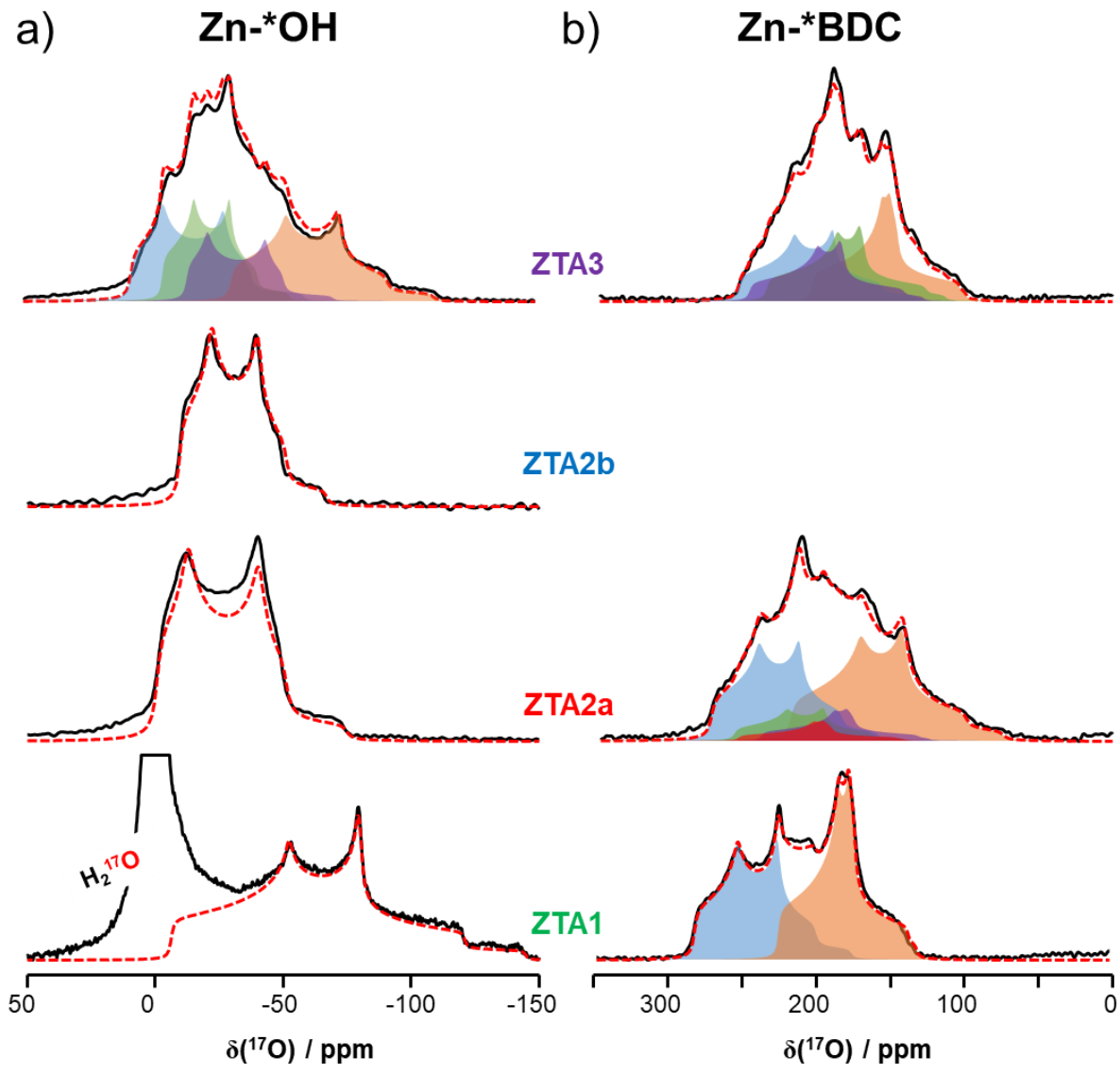

*Figure 4: ^{17}O MAS NMR spectra of ^{17}O-labelled Zn-BDC compounds prepared by mechanochemistry, B_0 = 14.1 T, ν_{rot} = 18 kHz and T = 0 °C. a) **ZTA-*OH** samples correspond to the enrichment of the hydroxyl/water groups. b) **ZTA-*BDC** samples corresponding to the enrichment of the BDC moiety. For all spectra, the red dotted line corresponds to the results of the fitting process.*

Regarding the **Zn-*OH** phases labelled on the hydroxyl/water positions, the NMR spectra were found to be generally easier to analyse (**Figure 4a**). Only one *OH site was observed for both **ZTA2a-*OH** and **ZTA2b-*OH**, as expected from the published crystal structures. In contrast, **ZTA3-*OH** was found to exhibit a more complex lineshape consisting of several inequivalent sites (**Figure 4a**). These were resolved using a ^{17}O MQMAS NMR experiment (see ESI **Figure S11**). Moreover, the OH network of this compound was further investigated through a ^{1}H-^{17}O dipolar correlation experiment, as detailed below (see **Figure 5**).

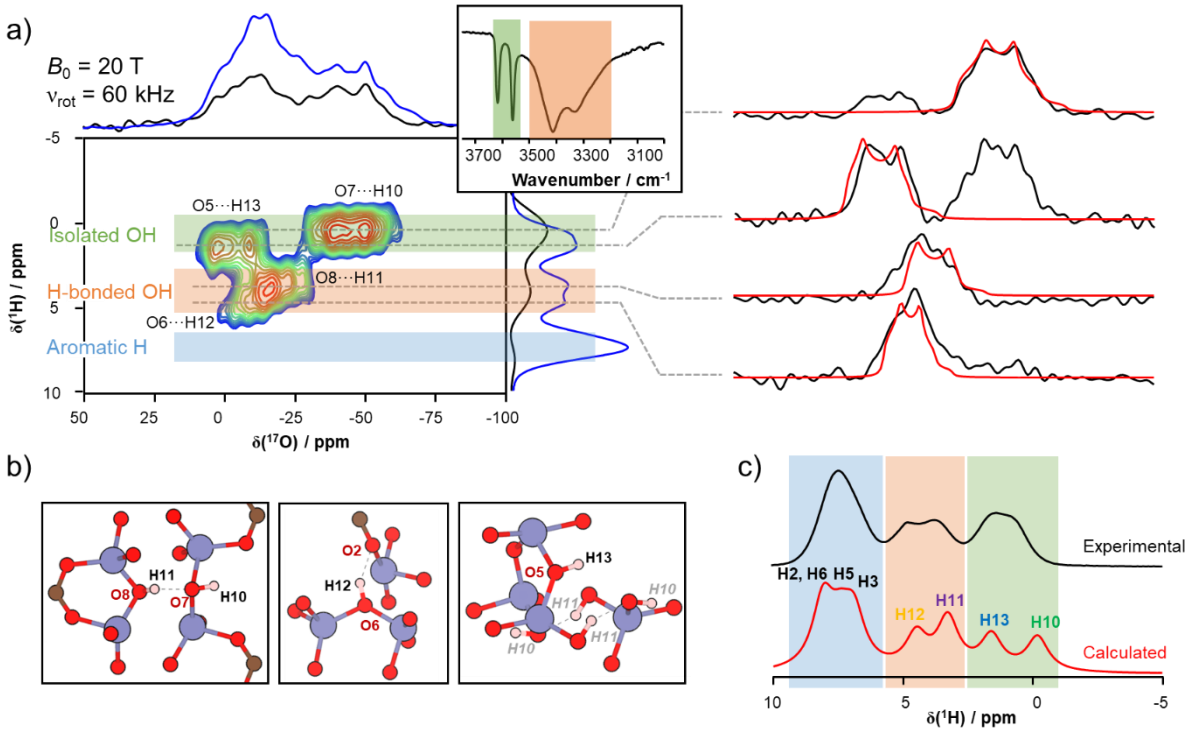

*Figure 5: a) ^{1}H-^{17}O D-HMQC of **ZTA3-*OH** recorded at 20.0 T under a spinning speed of 60 kHz. In blue are the ^{17}O and ^{1}H 1D spectra recorded in the same condition than the D-HMQC. The insert displays the FTIR spectrum centred on the OH stretching region. H-bonded OH groups are highlighted in orange, and isolated OH groups in green. b) DFT optimized **ZTA3** structure close views of the different hydroxyls environments, colour code: brown for carbon, red for oxygen, light pink for hydrogen and grey for zinc. c) Comparison of experimental ^{1}H MAS spectrum (recorded at B_0 = 20.0 T and ν_{rot} = 60 kHz) and simulated spectrum from calculated ^{1}H NMR parameters.*

The D-HMQC experiment allows the ^{1}H···^{17}O proximities to be probed, and turned out to be highly useful to help position the hydroxyl protons (which were absent from the initial X-ray diffraction data). Here, a short recoupling time was used (τ_{rec} = 100 µs), in order to observe the shortest O···H contacts (*i.e.* the O-H bonds). In these conditions, no correlation between hydroxyl oxygen atoms and aromatic

protons was observed (blue-shaded zone), but four environments could be resolved for the hydroxyls, one per inequivalent OH, in line with the published crystal structure (3 being μ_3-OH and 1 μ_2-OH). More interestingly, when looking at the FTIR spectrum of **ZTA3** (see insert **Figure 5a**), four environments of the hydroxyls could also be detected and separated in two groups: two for isolated OH species (green shaded zone) and two for OH species involved in H-bonding (orange shaded zone). A similar distinction can be made using the D-HMQC data. Indeed, the most shielded oxygen site ($\delta_{iso}(^{17}O)$ = -27.9 ppm) and most deshielded one ($\delta_{iso}(^{17}O)$ = 12.8 ppm) are correlated to ^{1}H resonances with low chemical shift (close to 0 ppm), such ^{1}H shifts being characteristic of isolated OH groups (zone shaded in green).[87], [88] On the other hand, the two remaining OH sites are correlated to ^{1}H resonances with $\delta_{iso}(^{1}H)$ close to 5 ppm, implying that they are involved in hydrogen bonds (orange shaded zone).[89]

Using these high-resolution ^{1}H-^{17}O experiments as a guideline, different configurations were tested to position the four hydroxyl hydrogens in the **ZTA3** structure, which were then geometry-optimized by DFT. The resulting GIPAW-DFT computed ^{1}H ssNMR spectrum of the best model is highly comparable to the high spinning speed ^{1}H NMR spectrum (**Figure 5c**). The resulting refined **ZTA3** structure exhibits two isolated hydroxyls: one (O5-H13) is shared between Zn3-Zn2-Zn3 (μ_3-OH), while the second one (O7-H10) is located between Zn1-Zn2 (μ_2-OH); both display a low $\delta_{iso}(^{1}H)$ chemical shift (1.34 and 0.80 ppm respectively). In contrast, the hydroxyl protons denoted H11 and H12 have a higher chemical shift, indicative of the presence of a hydrogen-bonding network, as can be seen in the geometry optimized structure (see **Figure 5b**): the H11⋯O7 and H12⋯O2 distances were found to be only ~ 1.7 Å.

Generally speaking, the calculated ^{17}O NMR parameters were found to be in satisfactory agreement with the ones extracted from experimental data. The overestimation of C_Q, often observed in **Table 5**, is consistent with what has been recently reported in the ^{17}O NMR literature on MOFs.[52], [90] However, unlike the calculated ^{13}C NMR parameters, no clear trend between ^{17}O NMR parameters and structural geometric parameters ($d_{C\text{-}O}$, $d_{Zn\cdots O}$, $\theta_{Zn\cdots O\text{-}C}$…) could be derived (see ESI **Figure S17** and **S18**). This is probably due to the multifactorial dependence between the ^{17}O NMR parameters and the local environment and geometry around the oxygen in these structures.

*Table 5: ^{17}O ssNMR parameters extracted from experimental spectra (**Figure 4**) recorded at multiple magnetic fields, and calculated using DFT from structural models of the phases.*

		Experimental				Calculated		
Enrichment	**Compound**	**$\delta_{iso}(^{17}O)$** / ppm	**C_Q**[a] / MHz	**η_Q**	**Int** / %	**$\delta_{iso}(^{17}O)$** / ppm	**C_Q** / MHz	**η_Q**
***OH**	**ZTA3**	12.8 ± 0.6	5.59 ± 0.02	0.30 ± 0.02	27.2	6.1	-7.88	0.64
		-1.9 ± 0.1	4.71 ± 0.04	0.43 ± 0.10	17.9	3.7	6.81	0.98
		-8.5 ± 0.1	5.22 ± 0.01	0.23 ± 0.02	23.6	0.4	-4.31	0.53
		-27.9 ± 0.2	5.92 ± 0.02	0.47 ± 0.01	31.3	-27.3	-7.98	0.51
	ZTA2b	-5.6 ± 0.4	5.10 ± 0.10	0.36 ± 0.01	100	-9.9	-5.92	0.33
	ZTA2a	5.5 ± 1.3	5.90 ± 0.12	0.25 ± 0.02	100	1.8	-6.89	0.34
	ZTA1	-3.2 ± 3.0	7.66 ± 0.20	0.61 ± 0.04	100	-15.8	9.32	0.49
***BDC**	**ZTA3**	258.4 ± 0.1	7.23 ± 0.01	0.56 ± 0.01	28.5	276.3	7.73	0.80
		249.0 ± 0.7	6.97 ± 0.02	0.74 ± 0.03	25.3	273.4	7.93	0.84
		237.3 ± 0.5	7.06 ± 0.01	0.75 ± 0.06	19.9	254.7	-6.77	0.97
		205.2 ± 0.8	6.39 ± 0.05	0.90 ± 0.10	26.3	210.2	-7.26	0.63
	ZTA2a	278.3 ± 1.6	7.07 ± 0.10	0.51 ± 0.11	32.3	298.1	7.37	0.69
		261.3 ± 1.0	7.04 ± 0.02	0.56 ± 0.13	10.5			
		255.7 ± 1.5	6.70 ± 0.21	0.88 ± 0.12	5.2			
		240.3 ± 5.3	6.74 ± 0.30	0.85 ± 0.15	8.7			
		223.0 ± 1.1	7.85 ± 0.05	0.60 ± 0.08	43.3	253.0	8.79	0.62
	ZTA1	286.6 ± 1.3	6.90 ± 0.05	0.46 ± 0.02	50.9	320.6	7.46	0.69
		221.7 ± 2.1	5.83 ± 0.49	0.85 ± 0.01	49.1	251.3	-6.71	0.67

[a] experimental C_Q values are given in absolute value

Concerning the phases enriched on the carboxylates, the experimental $\delta_{iso}(^{17}O)$ arising from the BDC* ligands of the different structures were found to span between 205.2 and 286.6 ppm (see **Figure 4b**). **ZTA1-*BDC** exhibits two clear inequivalent oxygen resonances, as expected from the crystal structure. On the contrary, **ZTA2a-*BDC** and **ZTA3-*BDC** gave more complex signatures, due to the presence of several overlapping resonances. The ^{17}O MAS NMR spectra of **ZTA3-*BDC** could for example be fitted considering the presence of 4 different ^{17}O signals, as expected from the crystal structure and resolved with the MQMAS experiments (see ESI **S12**). Concerning the **ZTA2a-*BDC**

phase, only 2 carboxylate oxygen resonances were expected according to the reported crystal structure. However, it was not possible to obtain a satisfactory simulated spectrum with only 2 signals. This result supports the observation made previously by ^{13}C NMR for **ZTA2a**, where an additional ^{13}C carboxylate resonance of weak intensity was detected at 172.5 ppm (see **Figure 3b**).

In order to learn more about the minor carboxylate environments in **ZTA2a**, the ^{17}O MQMAS spectrum of **ZTA2a-*BDC** was recorded (**Figure 6**). The two most intense resonances, which are centred at $\delta_{iso}(^{17}O)$ = 278.3 and 223.0 ppm, belong to the main carboxylate group (*i.e.* with the ^{13}C signal at 175.7 ppm). Yet, several signals of weaker intensity can also be observed (red shaded circle), corresponding to multiple and slightly different carboxylate local environments. Three examples of these additional oxygen environments were extracted from this area for further study (**Figure 6**, right).

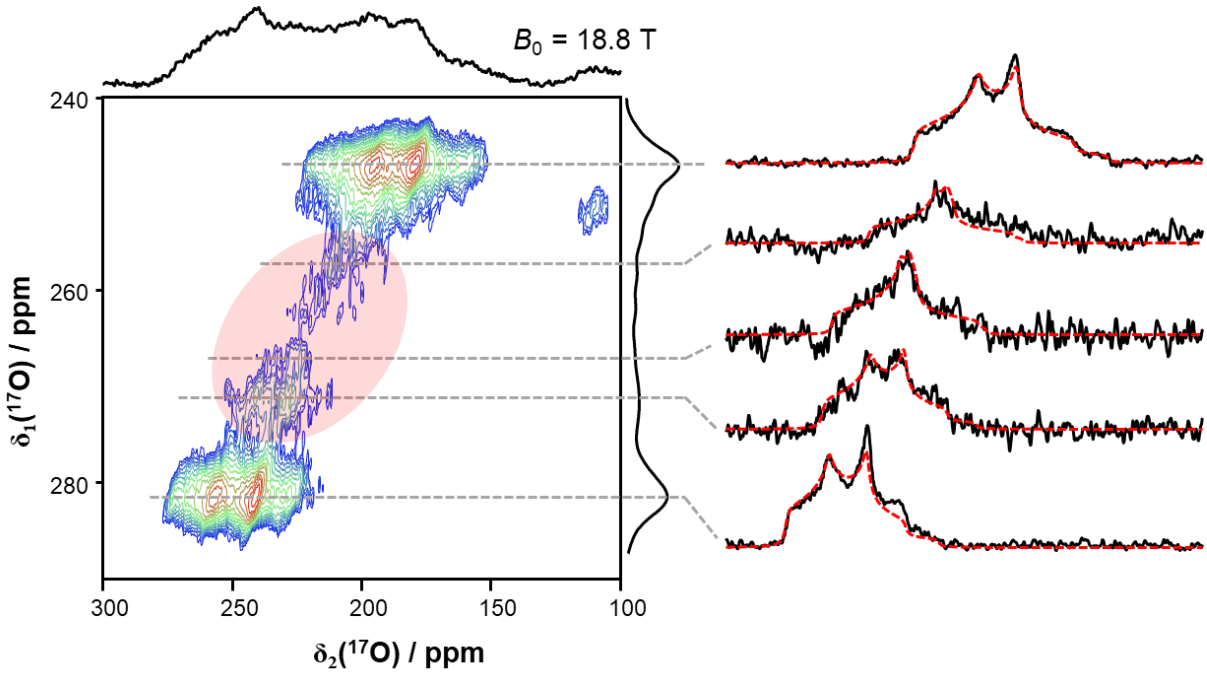

*Figure 6: ^{17}O MQMAS spectrum of **ZTA2a-*BDC** recorded at B_0 = 18.8 T under ν_{rot} = 16 kHz. Extracted slices are fitted with parameters presented in **Table 5**. The red shaded circle enlightens some of the additional oxygen sites.*

Despite their low signal-to-noise ratio, the signals from the three different slices could be tentatively fitted using quadrupolar lineshapes, suggesting that they correspond to carboxylate oxygens in a relatively well-ordered local environment. Using the NMR parameters derived from the different ^{17}O environments resolved by MQMAS, it was then possible to propose a fit of the ^{17}O NMR spectra of

ZTA2a-*BDC in the carboxylate region (see **Figure 4b** and **Table 5**). However, it should be kept in mind that additional weak-intensity carboxylate resonances may also be overlapping with the two main resonances (which remained unresolved at this stage). Interestingly, the ^{17}O NMR data also shows that the main resonances for **ZTA2a-*BDC** ($\delta_{iso}(^{17}O)$ = 278.3 and 223.0 ppm) are relatively close in shift to the ones of **ZTA1-*BDC** ($\delta_{iso}(^{17}O)$ = 286.6 and 221.7 ppm), further underscoring the similarities between ^{17}O ssNMR and ^{13}C ssNMR parameters ($\delta_{iso}(^{17}O)$, $\delta_{iso}(^{13}COO)$ and ^{13}C CSA) for the two different binding modes, *i.e. syn,syn/anti* bridging (**ZTA2a**) and monodentate (**ZTA1**). Regarding the weaker signals (red circles on **Figure 6**), they are likely to arise from the presence of the systematic defects inside the crystallographic structure, as already hinted from the ^{13}C NMR data.

Thanks to the selective ^{17}O-labelling of the various Zn-BDC compounds by BM, it was possible to gain novel insights into the local environment of the oxygen-containing ligands, as well as refine one of the crystallographic structures (**ZTA3**) by DFT-calculations. Although no straightforward trend relating ^{17}O NMR parameters to carboxylate binding modes could be derived, most probably because of the influence of several geometrical features (Zn···O and O-C distances, bond angles, positioning of neighbouring ligands...), high resolution ^{17}O ssNMR spectroscopy, in conjunction with DFT calculations and GIPAW calculations of NMR parameters clearly appear as a crucial asset to help confirm the structural models of these types of MOFs. In particular, they will be useful in the future to help elucidate the nature of the defect sites in **ZTA2a**, in an NMR-crystallography type of approach.[91]

Outlook: isotope labelling for simplified in situ observations of evolutions in the reaction media

Because structural rearrangements occur around the water molecules/hydroxyls during the Zn-BDC transformations described above, being able to follow this by Raman spectroscopy appeared to us as an important goal, in order to increase our insight into the transformations taking place. Unfortunately, it was not possible to follow the evolution of the O-H stretching modes upon synthesis by BM with our Raman set-up, because it only allowed spectra to be recorded from 220 to 3120 cm^{-1}, while ν(OH) most-often appear at higher wavenumbers.[92]–[94]

To circumvent this issue, we thus decided to perform isotope labelling of Zn-BDC phases using deuterium oxide rather than normal water as a starting material in the syntheses. In doing so, the stretching modes arising from -OH groups would correspond to -OD groups, which can be observed between 2400 and 2800 cm^{-1}. **Figure 7** presents as an example the result of a synthesis followed by *operando* Raman spectroscopy, and performed using an initial Zn/BDC ratio of 3/1, and D_2O instead of H_2O. The corresponding temperature measurement through the thermal imaging camera is placed on the side of the Raman spectra (**Figure 7a**), and the focus of the Raman data is set in the zone between 2600 and 2700 cm^{-1}, where O-D stretching vibrations appear.

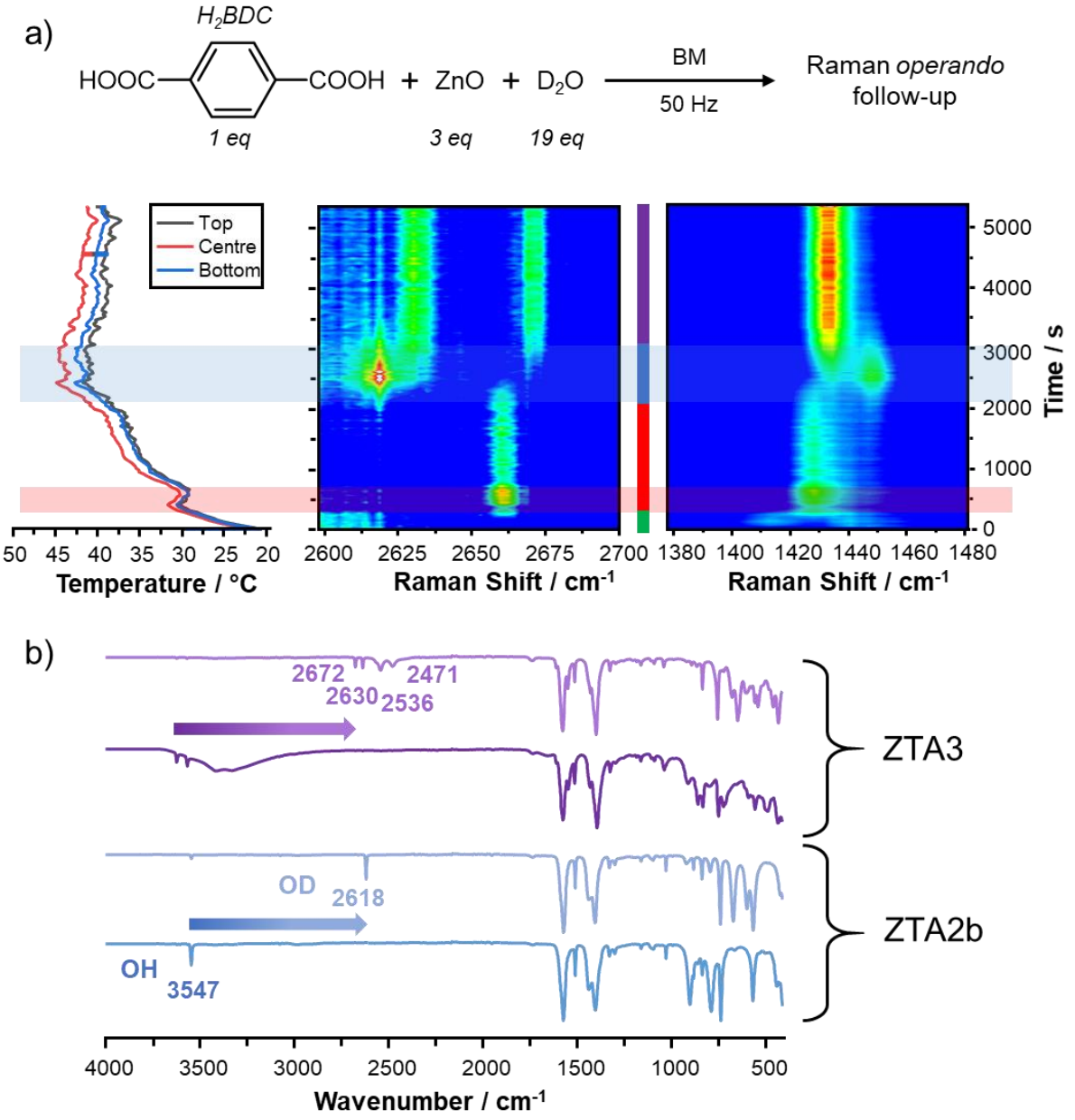

*Figure 7: a) Top: Starting compounds used for the operando experiment with their respective equivalents, Bottom: Time-resolved operando Raman spectra of two selected areas: 2600-2700 cm^{-1} range on the left and 1380-1480 cm^{-1} range on the right, following the Raman spectroscopy convention for displaying the data (high wavenumbers on the right). The graph on the far left corresponds to the temperature measurement recorded using the thermal imaging camera. b) Experimental ex situ FTIR spectra of **ZTA2b** (in blue), **ZTA2b-OD** (in light blue), **ZTA3** (in purple) and **ZTA3-OD** (in light purple), following the FTIR spectroscopy convention for displaying the data (high wavenumbers on the left).*

The formation and transformation of the intermediates is noticeable through the change in temperature, as well as the modifications of the Raman spectra. It should be noted that no signal from **ZTA1** was observed in the 2600-2700 cm^{-1} area (**Figure 7**), because of the lack of isolated OH environments in this phase, the water molecules being involved in hydrogen bonds. The broad signal

arising from these water molecules is indeed too weak to be detected during the *operando* Raman experiment. Hence, in the 2600-2700 cm^{-1} range, when working with a 3/1 Zn/BDC ratio in D_2O, we observed first the formation of the **ZTA2a-OD**, through the presence of the ν(OD) band (2660 cm^{-1}). As with the synthesis presented in **Figure 1**, it then transforms into the **ZTA2b-OD** structure (2618 cm^{-1}). Then, the excess of zinc oxide allows the formation of the **ZTA3-OD** compound as the final form (ν(OD) = 2630 & 2671 cm^{-1}). This final phase has a Zn/BDC stoichiometry of 3/1, consistent with the one between the reagents introduced in the jar. It is worth noting that we were able to observe the 2 distinct O-D bands in the final compound, corresponding to the expected 2 isolated hydroxyls (Zn-O(H)-Zn).

The interest of using deuterated precursors for *operando* Raman mechanochemistry was further demonstrated here, by using ring-d_4 terephthalic acid as a starting reagent. In doing so, the ν(CH) Raman signals become ν(CD) signals, which, in the case of **ZTA1** for example, corresponds to a shift of the stretching vibrations from at 3064 and 3105 cm^{-1} to 2287 and 2321 cm^{-1} (see ESI **Figure S19**).[95] Therefore, isotope labelling by deuteration can be seen as a way of shifting Raman vibrations in an area of the spectrum were no signal from the jar is expected, allowing a more straightforward observation of the evolving vibration modes as well as an easier post-synthesis data treatment. Both methods, using D_2O or d_4-BDC, can also be combined in order to study the change of kinetics for such reactions. Overall, this demonstrates, beyond the study of reaction mechanisms in ball-milling,[96] how isotopic labelling by deuteration, can be particularly useful also for following the kinetics in mechanochemical reactions, by shifting vibration bands into regions where they become detectable (*e.g.* OD *vs.* OH), and/or to avoid overlaps with other vibration frequencies (including from the jar). Such strategies may also turn out to be particularly valuable to refine kinetic data which may be ambiguous in other regions (as highlighted at the beginning of this manuscript), and thereby help elucidate complex mechanochemical reactions.

Conclusion

In this contribution, we have performed the first in-depth study of the formation and structure of four coordination polymers involving Zn^{2+} cations and terephthalate ligands, denoted **ZTA1**, **ZTA2a**, **ZTA2b** and **ZTA3**. Although each of these phases had been previously reported independently (for instance as part of investigations aiming at studying the formation of the well-known MOF-5 structure), the details of their structure, and in the case of **ZTA2a** the possibility to isolate it as phase-pure, were missing. Here, it is shown for the first time how using mechanochemistry, in conjunction with *operando* Raman spectroscopy and thermal imaging, the evolution of the reaction medium could be followed. Each of the phases could be isolated as pure, either by adapting the stoichiometry of the Zn and BDC precursors involved in the milling, or by stopping the milling synthesis at a specific timepoint, based on knowledge of the kinetics of the reactions. Beyond the fact that for some of these phases, this is the first time that they are prepared by BM (*e.g.* **ZTA3**), it is important to highlight that in the case of **ZTA2a**, no synthetic procedure had been reported to date enabling phase pure preparation, making our mechanochemical approach particularly valuable. Moreover, the study of the formation of **ZTA3** by mechanochemistry was shown to proceed through the successive formation of the **ZTA1**, **ZTA2a** and **ZTA2b** intermediates, a process during which the carboxylate ligands progressively switch from monodentate (**ZTA1**) to weakly bridging (**ZTA2a,** in a *syn,syn/anti* configuration) and finally into stronger bidentate coordination modes towards Zn^{2+} cations (**ZTA2b** and **ZTA3**), while coordinated water molecules (**ZTA1**) deprotonate to form bridging hydroxyl ligands, some of which eventually relate to each other through an H-bonding network (**ZTA3**) (see **Figure 8**).

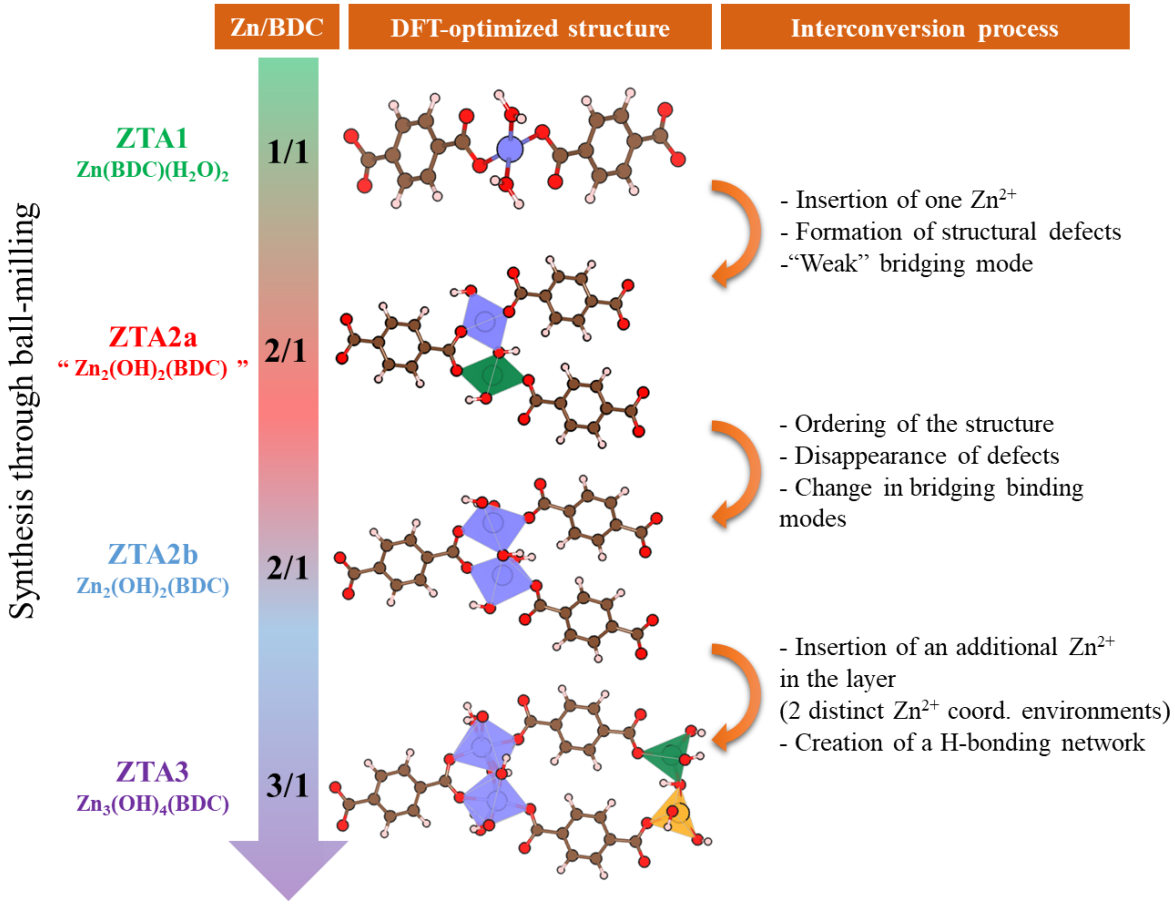

Figure 8: Summary of the structural evolution of the Zn-BDC compounds presented in this article upon milling synthesis. The molecular schemes arise from the DFT-optimized structures obtained in this article.

For each of the phases, an NMR-crystallography approach was then used, combining high-resolution NMR spectroscopy with *ab initio* DFT calculations of NMR parameters, in order to help refine the crystal structures, as much information was lacking in the crystallographic data available to date. Notably, the combination of ^{13}C and ^{17}O NMR experiments was used in order to apprehend the local information concerning the binding modes of the terephthalate ligands to the Zn^{2+} cations. Regarding ^{13}C ssNMR, a systematically lower $\delta_{iso}(^{13}COO)$ was observed for *syn,syn* bridging ligands as opposed to monodentate and weaker *syn,syn/anti* bridging modes (~ 4 ppm difference in shifts). Moreover, $\delta_{iso}(^{13}COO)$ and the CSA span (Ω) parameter were found to correlate reasonably well with the longest C-O distance of the carboxylate, making the measurement of these parameters valuable for extracting structural information in future studies of other unknown Zn-terephthalate coordination

networks. Furthermore, the ^{13}C ssNMR study allowed an additional carboxylate resonance to be detected for the **ZTA2a** compound reflecting the likely presence of "defect" in that structure.

Regarding ^{17}O ssNMR, the key point to highlight is that using the protocols developed here by mechanochemistry, it was possible to produce selectively ^{17}O-labelled phases in high yield, with either enriched hydroxyls (Zn-O*(H)-Zn) or enriched carboxylates (CO*O*-Zn). Such selective labelling was possible because reactions were performed here by BM under "ambient" temperature and pressure, and short times (less than 3 hours). Moreover, it is important to highlight that the syntheses of these ^{17}O-enriched compounds would have been far too expensive if not for the BM procedures optimized through the use of real-time monitoring Raman spectroscopy. Indeed, the extent of enriched H_2O* employed here was very low (for **Zn-O*H**, ~ 45 µL for ~ 300 mg of sample recovered and ~ 20 µL for ~ 110 mg of sample recovered for **Zn-BDC***), and could not have been matched for syntheses carried out using the hydrothermal or microwave procedures proposed so far to prepare such compounds. Thanks to this isotopic labelling, high-resolution ^{17}O ssNMR spectra could be recorded for each of the phases in just a few hours, allowing different carboxylate-oxygen and hydroxyl environments to be resolved. This allowed, for example, a very precise positioning of hydroxyl-hydrogens in the case of the **ZTA3** phase. Regarding terephthalate ligands, however, no straightforward correlation between ^{17}O NMR parameters and geometric features around the carboxylate oxygens could be derived, showing that the ^{17}O data in these phases is very sensitive to the local environment of oxygen, and depends on many different factors (*e.g.*, bond distances, angles). This implies that combined experimental-computational approaches involving various NMR-active nuclei, including ^{17}O, is a very valuable tool for validating structural models (and notably carboxylate binding modes) of these materials.

Among the four phases studied, the **ZTA2a** compound was proven to present a more complex structure than the one reported, with the probable presence of "defect" sites, as evidenced from both ^{13}C and ^{17}O ssNMR analyses. For this phase, the main terephthalate coordination mode seems to be a *syn,syn/anti* bridging mode with the two $d_{Zn\cdots O}$ distances from the same oxygen (*syn,syn* and *syn,anti)* longer (2.21 and 2.28 Å) than the $d_{Zn\cdots O}$ involved in the classic *syn,syn* bridging mode (between 1.98 and 2.17 Å). The defect sites, on the other hand, may correspond to terephthalate ligands with bridging

modes, but with shorter maxima $d(C\text{-}O)_1$ distances compared to the main carboxylate site, and a binding mode more similar to the ones found in **ZTA2b** and **ZTA3**, based on the $\delta_{iso}(^{13}C)$ value. Such information will serve as the basis for proposing structural models of these defects, which can then be validated using DFT calculations of NMR parameters. More generally speaking, considering the increasing number of studies on MOF structures which highlight the importance of further refining structural data (beyond what is possible by using powder X-ray diffraction), and to establish the nature and role of defects on reactivity, the possibility of using approaches such as the ones proposed herein, including selective ^{17}O isotopic, appears very valuable.

Lastly, through the study of the mechanochemical formation of the four Zn-BDC phases using *operando* Raman spectroscopy, we also demonstrate here for the first time how the use of deuterated precursors can be useful to help follow the course of the reactions, by enabling the observation of specific vibration modes (*e.g.* ν(OD) and/or ν(CD)), and thereby avoiding cut-off of high wavenumbers of the ν(OH) and/or ν(CH) modes, due to instrumentation, and/or avoiding their overlap with signal arising from the milling jar in the Raman spectra. We foresee that on a more general perspective, the study of deuterated compounds in *operando* Raman investigations by BM will be particularly useful to refine the understanding of the reactions occurring in the jars, and may enable the more straightforward investigation and optimization of reactions which not only concern the formation of MOFs, but may actually more specifically involve the formation of C-D (instead of C-H) bonds, as it is the case in reduction reactions in organic chemistry.

Acknowledgments

This project has received funding from the European Research Council (ERC) under the European Union's Horizon 2020 research and innovation programme (grant agreement No 772204; 2017 ERC-COG, MISOTOP project). DFT calculations were performed using HPC resources from GENCI-IDRIS (Grant 097535 and 2020-A0090807394). We are grateful to Prof. Franziska Emmerling for discussions regarding the Raman *operando* set-up, and for providing the Perspex jars used for the real-time monitoring synthesis. Sebastien Mittelette as well as the Mecanox summer school participants are thanked for providing the ^{17}O-enriched H_2BDC. We thank Drs. Ieva Goldberga and Philippe Gaveau for assistance in running some of the ssNMR experiments. A portion of this work was performed at the National High Magnetic Field Laboratory, which is supported by the National Science Foundation Cooperative Agreement No. DMR-1644779 and the State of Florida. Financial support from the IR-RMN-THC FR 3050 CNRS for conducting part of the NMR research at the CEMHTI facility in Orléans is gratefully acknowledged.

Author contributions

The project was conducted by CL, in close interaction with DL, TXM and CG. TXM, CL, and DL developed together the *operando* Raman spectroscopy set-up coupled to mechanochemistry. CL performed all BM syntheses, all characterizations by IR, Raman and pXRD, and the vast majority of ssNMR analyses. IH and ZG performed part of the high-field ^{17}O NMR experiments reported herein (MagLab). CG carried out the computational simulations and GIPAW DFT calculations. CL performed the data analyses, and prepared all figures and tables. CL and DL wrote the initial draft of the manuscript. All authors discussed the results and contributed to the final preparation of the manuscript.

References

[1] S. Boulineau, M. Courty, J.-M. Tarascon, and V. Viallet, "Mechanochemical synthesis of Li-argyrodite Li_6PS_5X (X=Cl, Br, I) as sulfur-based solid electrolytes for all solid state batteries application," *Solid State Ionics*, vol. 221, pp. 1–5, Aug. 2012, doi: 10.1016/j.ssi.2012.06.008.

[2] T. Friščić, C. Mottillo, and H. M. Titi, "Mechanochemistry for Synthesis," *Angew. Chem., Int. Ed.*, vol. 59, no. 3, pp. 1018–1029, Jan. 2020, doi: 10.1002/anie.201906755.

[3] J.-L. Do and T. Friščić, "Mechanochemistry: A Force of Synthesis," *ACS Cent. Sci.*, vol. 3, no. 1, pp. 13–19, Jan. 2017, doi: 10.1021/acscentsci.6b00277.

[4] D. Tan and F. García, "Main group mechanochemistry: from curiosity to established protocols," *Chem. Soc. Rev.*, vol. 48, no. 8, pp. 2274–2292, 2019, doi: 10.1039/C7CS00813A.

[5] D. Gracin, V. Štrukil, T. Friščić, I. Halasz, and K. Užarević, "Laboratory Real-Time and In Situ Monitoring of Mechanochemical Milling Reactions by Raman Spectroscopy," *Angew. Chem.*, vol. 126, no. 24, pp. 6307–6311, Jun. 2014, doi: 10.1002/ange.201402334.

[6] K. Užarević, I. Halasz, and T. Friščić, "Real-Time and In Situ Monitoring of Mechanochemical Reactions: A New Playground for All Chemists," *J. Phys. Chem. Lett.*, vol. 6, no. 20, pp. 4129–4140, Oct. 2015, doi: 10.1021/acs.jpclett.5b01837.

[7] L. Batzdorf, F. Fischer, M. Wilke, K.-J. Wenzel, and F. Emmerling, "Direct In Situ Investigation of Milling Reactions Using Combined X-ray Diffraction and Raman Spectroscopy," *Angew. Chem., Int. Ed.*, vol. 54, no. 6, pp. 1799–1802, Feb. 2015, doi: 10.1002/anie.201409834.

[8] F. Fischer, K.-J. Wenzel, K. Rademann, and F. Emmerling, "Quantitative determination of activation energies in mechanochemical reactions," *Phys. Chem. Chem. Phys.*, vol. 18, no. 33, pp. 23320–23325, 2016, doi: 10.1039/C6CP04280E.

[9] H. Kulla, S. Greiser, S. Benemann, K. Rademann, and F. Emmerling, "In Situ Investigation of a Self-Accelerated Cocrystal Formation by Grinding Pyrazinamide with Oxalic Acid," *Molecules*, vol. 21, no. 7, p. 917, Jul. 2016, doi: 10.3390/molecules21070917.

[10] S. Haferkamp, F. Fischer, W. Kraus, and F. Emmerling, “Mechanochemical Knoevenagel condensation investigated in situ,” *Beilstein J. Org. Chem.*, vol. 13, pp. 2010–2014, Sep. 2017, doi: 10.3762/bjoc.13.197.

[11] S. Lukin *et al.*, “Tandem In Situ Monitoring for Quantitative Assessment of Mechanochemical Reactions Involving Structurally Unknown Phases,” *Chem. - A Eur. J.*, vol. 23, no. 56, pp. 13941–13949, Oct. 2017, doi: 10.1002/chem.201702489.

[12] V. Štrukil, D. Gracin, O. V. Magdysyuk, R. E. Dinnebier, and T. Friščić, “Trapping Reactive Intermediates by Mechanochemistry: Elusive Aryl N -Thiocarbamoylbenzotriazoles as Bench-Stable Reagents,” *Angew. Chem., Int. Ed.*, vol. 54, no. 29, pp. 8440–8443, Jul. 2015, doi: 10.1002/anie.201502026.

[13] S. Lukin *et al.*, “Mechanochemical carbon–carbon bond formation that proceeds via a cocrystal intermediate,” *Chem. Commun.*, vol. 54, no. 94, pp. 13216–13219, 2018, doi: 10.1039/C8CC07853J.

[14] H. Kulla, M. Wilke, F. Fischer, M. Röllig, C. Maierhofer, and F. Emmerling, “Warming up for mechanosynthesis – temperature development in ball mills during synthesis,” *Chem. Commun.*, vol. 53, no. 10, pp. 1664–1667, 2017, doi: 10.1039/C6CC08950J.

[15] H. Kulla *et al.*, “In Situ Investigations of Mechanochemical One-Pot Syntheses,” *Angew. Chem., Int. Ed.*, vol. 57, no. 20, pp. 5930–5933, May 2018, doi: 10.1002/anie.201800147.

[16] M. Carta, E. Colacino, F. Delogu, and A. Porcheddu, “Kinetics of mechanochemical transformations,” *Phys. Chem. Chem. Phys.*, vol. 22, no. 26, pp. 14489–14502, 2020, doi: 10.1039/D0CP01658F.

[17] I. Sović *et al.*, “Mechanochemical Preparation of Active Pharmaceutical Ingredients Monitored by In Situ Raman Spectroscopy,” *ACS Omega*, vol. 5, no. 44, pp. 28663–28672, Nov. 2020, doi: 10.1021/acsomega.0c03756.

[18] R. J. Kuppler *et al.*, “Potential applications of metal-organic frameworks,” *Coord. Chem. Rev.*,

vol. 253, no. 23–24, pp. 3042–3066, Dec. 2009, doi: 10.1016/j.ccr.2009.05.019.

[19] Y. Sakamaki *et al.*, "Metal–Organic Frameworks and Covalent Organic Frameworks as Platforms for Photodynamic Therapy," *Comments Inorg. Chem.*, vol. 38, no. 6, pp. 238–293, Nov. 2018, doi: 10.1080/02603594.2018.1542597.

[20] T. Ghanbari, F. Abnisa, and W. M. A. Wan Daud, "A review on production of metal organic frameworks (MOF) for CO_2 adsorption," *Sci. Total Environ.*, vol. 707, p. 135090, Mar. 2020, doi: 10.1016/j.scitotenv.2019.135090.

[21] N. Stock and S. Biswas, "Synthesis of Metal-Organic Frameworks (MOFs): Routes to Various MOF Topologies, Morphologies, and Composites," *Chem. Rev.*, vol. 112, no. 2, pp. 933–969, Feb. 2012, doi: 10.1021/cr200304e.

[22] Y.-R. Lee, J. Kim, and W.-S. Ahn, "Synthesis of metal-organic frameworks: A mini review," *Korean J. Chem. Eng.*, vol. 30, no. 9, pp. 1667–1680, Sep. 2013, doi: 10.1007/s11814-013-0140-6.

[23] N. Zhao, K. Cai, and H. He, "The synthesis of metal–organic frameworks with template strategies," *Dalton Trans.*, vol. 49, no. 33, pp. 11467–11479, 2020, doi: 10.1039/D0DT01879A.

[24] T. Stolar and K. Užarević, "Mechanochemistry: an efficient and versatile toolbox for synthesis, transformation, and functionalization of porous metal–organic frameworks," *CrystEngComm*, vol. 22, no. 27, pp. 4511–4525, 2020, doi: 10.1039/D0CE00091D.

[25] C. Lin *et al.*, "Digital Control of Multistep Hydrothermal Synthesis by Using 3D Printed Reactionware for the Synthesis of Metal–Organic Frameworks," *Angew. Chem.*, vol. 130, no. 51, pp. 16958–16962, Dec. 2018, doi: 10.1002/ange.201810095.

[26] C. L. Jones, C. E. Hughes, H. H. M. Yeung, A. Paul, K. D. M. Harris, and T. L. Easun, "Exploiting in situ NMR to monitor the formation of a metal–organic framework," *Chem. Sci.*, vol. 12, no. 4, pp. 1486–1494, 2021, doi: 10.1039/D0SC04892E.

[27] B. Karadeniz *et al.*, "Controlling the Polymorphism and Topology Transformation in Porphyrinic

Zirconium Metal–Organic Frameworks via Mechanochemistry," *J. Am. Chem. Soc.*, vol. 141, no. 49, pp. 19214–19220, Dec. 2019, doi: 10.1021/jacs.9b10251.

[28] Y. Qin *et al.*, "Additive manufacturing of biodegradable Zn-xWE43 porous scaffolds: Formation quality, microstructure and mechanical properties," *Mater. Des.*, vol. 181, p. 107937, Nov. 2019, doi: 10.1016/j.matdes.2019.107937.

[29] E. K. Arabbaghi, J. Mokhtari, M. R. Naimi-Jamal, and A. Khosravi, "Zn-MOF: an efficient drug delivery platform for the encapsulation and releasing of Imatinib Mesylate," *J. Porous Mater.*, vol. 28, no. 2, pp. 641–649, Apr. 2021, doi: 10.1007/s10934-020-01027-3.

[30] A. Karmakar, M. F. C. Guedes da Silva, and A. J. L. Pombeiro, "Zinc metal–organic frameworks: efficient catalysts for the diastereoselective Henry reaction and transesterification," *Dalton Trans.*, vol. 43, no. 21, pp. 7795–7810, 2014, doi: 10.1039/C4DT00219A.

[31] L. Wang *et al.*, "Zinc terephthalates $ZnC_8H_4O_4$ as anodes for lithium ion batteries," *Electrochim. Acta*, vol. 235, pp. 304–310, May 2017, doi: 10.1016/j.electacta.2017.03.095.

[32] X. Qin, W. Yang, Y. Yang, D. Gu, D. Guo, and Q. Pan, "A Zinc Metal–Organic Framework for Concurrent Adsorption and Detection of Uranium," *Inorg. Chem.*, vol. 59, no. 14, pp. 9857–9865, Jul. 2020, doi: 10.1021/acs.inorgchem.0c01072.

[33] N. Getachew, Y. Chebude, I. Diaz, and M. Sanchez-Sanchez, "Room temperature synthesis of metal organic framework MOF-2," *J. Porous Mater.*, vol. 21, no. 5, pp. 769–773, Oct. 2014, doi: 10.1007/s10934-014-9823-6.

[34] J. Xing, L. Schweighauser, S. Okada, K. Harano, and E. Nakamura, "Atomistic structures and dynamics of prenucleation clusters in MOF-2 and MOF-5 syntheses," *Nat. Commun.*, vol. 10, no. 1, p. 3608, Dec. 2019, doi: 10.1038/s41467-019-11564-4.

[35] L. Schweighauser, K. Harano, and E. Nakamura, "Experimental study on interconversion between cubic MOF-5 and square MOF-2 arrays," *Inorg. Chem. Commun.*, vol. 84, no. 3, pp. 1–4, Oct. 2017, doi: 10.1016/j.inoche.2017.07.009.

[36] M. Edgar, R. Mitchell, A. M. Z. Slawin, P. Lightfoot, and P. A. Wright, “Solid-State Transformations of Zinc 1,4-Benzenedicarboxylates Mediated by Hydrogen-Bond-Forming Molecules,” *Chem. - A Eur. J.*, vol. 7, no. 23, p. 5168, Dec. 2001, doi: 10.1002/1521-3765(20011203)7:23<5168::AID-CHEM5168>3.3.CO;2-J.

[37] Y. Hirai *et al.*, “Microwave-assisted hydrothermal synthesis of ZnO and Zn-terephthalate hybrid nanoparticles employing benzene dicarboxylic acids,” *Microsyst. Technol.*, vol. 24, no. 1, pp. 699–708, Jan. 2018, doi: 10.1007/s00542-017-3392-y.

[38] S. Geranmayeh, A. Abbasi, A.-H. Zarnani, and M. Y. Skripkin, “A novel trinuclear zinc metal–organic network: Synthesis, X-ray diffraction structures, spectroscopic and biocompatibility studies,” *Polyhedron*, vol. 61, pp. 6–14, Sep. 2013, doi: 10.1016/j.poly.2013.05.030.

[39] L.-N. Zhu *et al.*, “$[Zn(BDC)(H_2O)_2]_n$: a novel blue luminescent coordination polymer constructed from BDC-bridged 1-D chains via interchain hydrogen bonds (BDC=1,4-benzenedicarboxylate),” *Inorg. Chem. Commun.*, vol. 5, no. 12, pp. 1017–1021, Dec. 2002, doi: 10.1016/S1387-7003(02)00634-2.

[40] G. Guilera and J. W. Steed, “Topological control in coordination polymers by non-covalent forces,” *Chem. Commun.*, vol. 2, no. 16, pp. 1563–1564, 1999, doi: 10.1039/a903163d.

[41] J. A. Kaduk, *CSD Commun.*, 2016, doi: 10.5517/ccdc.csd.cc1n13d6.

[42] A. Carton, A. Mesbah, L. Aranda, P. Rabu, and M. François, “New metastable hybrid phase, $Zn_2(OH)_2(C_8H_4O_4)$, exhibiting unique oxo-penta-coordinated Zn(II) atoms,” *Solid State Sci.*, vol. 11, no. 4, pp. 818–823, Apr. 2009, doi: 10.1016/j.solidstatesciences.2008.12.011.

[43] A. Carton, S. Abdelouhab, G. Renaudin, P. Rabu, and M. François, “Structure of zinc hydroxy-terephthalate: $Zn_3(OH)_{4(}C_8H_4O_4)$,” *Solid State Sci.*, vol. 8, no. 8, pp. 958–963, Aug. 2006, doi: 10.1016/j.solidstatesciences.2006.02.043.

[44] N. A. Rodríguez, R. Parra, and M. A. Grela, “Structural characterization, optical properties and photocatalytic activity of MOF-5 and its hydrolysis products: implications on their excitation

mechanism," *RSC Adv.*, vol. 5, no. 89, pp. 73112–73118, 2015, doi: 10.1039/C5RA11182J.

[45] A. Thirumurugan and C. N. R. Rao, "1,2-, 1,3- and 1,4-Benzenedicarboxylates of Cd and Zn of different dimensionalities: Process of formation of the three-dimensional structure," *J. Mater. Chem.*, vol. 15, no. 35–36, p. 3852, 2005, doi: 10.1039/b504666a.

[46] V. Zeleňák, Z. Vargová, and K. Györyová, "Correlation of infrared spectra of zinc(II) carboxylates with their structures," *Spectrochim. Acta Part A Mol. Biomol. Spectrosc.*, vol. 66, no. 2, pp. 262–272, Feb. 2007, doi: 10.1016/j.saa.2006.02.050.

[47] K. I. Hadjiivanov *et al.*, "Power of Infrared and Raman Spectroscopies to Characterize Metal-Organic Frameworks and Investigate Their Interaction with Guest Molecules," *Chem. Rev.*, vol. 121, no. 3, pp. 1286–1424, Feb. 2021, doi: 10.1021/acs.chemrev.0c00487.

[48] H. A. Habib, A. Hoffmann, H. A. Höppe, and C. Janiak, "Crystal structures and solid-state CPMAS ^{13}C NMR correlations in luminescent zinc(II) and cadmium(II) mixed-ligand coordination polymers constructed from 1,2-bis(1,2,4-triazol-4-yl)ethane and benzenedicarboxylate," *Dalton Trans.*, no. 10, p. 1742, 2009, doi: 10.1039/b812670d.

[49] W. Yuan, T. Friščić, D. Apperley, and S. L. James, "High Reactivity of Metal-Organic Frameworks under Grinding Conditions: Parallels with Organic Molecular Materials," *Angew. Chem., Int. Ed.*, vol. 49, no. 23, pp. 3916–3919, May 2010, doi: 10.1002/anie.200906965.

[50] P. A. Julien *et al.*, "In Situ Monitoring and Mechanism of the Mechanochemical Formation of a Microporous MOF-74 Framework," *J. Am. Chem. Soc.*, vol. 138, no. 9, pp. 2929–2932, Mar. 2016, doi: 10.1021/jacs.5b13038.

[51] X. Kong *et al.*, "Solid-State ^{17}O NMR Spectroscopy of Paramagnetic Coordination Compounds," *Angew. Chem., Int. Ed.*, vol. 54, no. 16, pp. 4753–4757, Apr. 2015, doi: 10.1002/anie.201409888.

[52] G. P. M. Bignami *et al.*, "Cost-effective ^{17}O enrichment and NMR spectroscopy of mixed-metal terephthalate metal–organic frameworks," *Chem. Sci.*, vol. 9, no. 4, pp. 850–859, 2018, doi: 10.1039/C7SC04649A.

[53] J. Špačková *et al.*, "Unveiling the Structure and Reactivity of Fatty-Acid Based (Nano)materials Thanks to Efficient and Scalable ^{17}O and ^{18}O-Isotopic Labeling Schemes," *J. Am. Chem. Soc.*, vol. 142, no. 50, pp. 21068–21081, Dec. 2020, doi: 10.1021/jacs.0c09383.

[54] S. E. Ashbrook, Z. H. Davis, R. E. Morris, and C. M. Rice, "^{17}O NMR spectroscopy of crystalline microporous materials," *Chem. Sci.*, vol. 12, no. 14, pp. 5016–5036, 2021, doi: 10.1039/D1SC00552A.

[55] V. Martins *et al.*, "Higher Magnetic Fields, Finer MOF Structural Information: ^{17}O Solid-State NMR at 35.2 T," *J. Am. Chem. Soc.*, vol. 142, no. 35, pp. 14877–14889, Sep. 2020, doi: 10.1021/jacs.0c02810.

[56] T.-X. Métro, C. Gervais, A. Martinez, C. Bonhomme, and D. Laurencin, "Unleashing the Potential of ^{17}O NMR Spectroscopy Using Mechanochemistry," *Angew. Chem., Int. Ed.*, vol. 56, no. 24, pp. 6803–6807, Jun. 2017, doi: 10.1002/anie.201702251.

[57] C.-H. Chen *et al.*, "Direct ^{17}O Isotopic Labeling of Oxides Using Mechanochemistry," *Inorg. Chem.*, vol. 59, no. 18, pp. 13050–13066, Sep. 2020, doi: 10.1021/acs.inorgchem.0c00208.

[58] C.-H Chen *et al.*, "Looking into the dynamics of molecular crystals of ibuprofen and terephthalic acid using ^{17}O and ^{2}H nuclear magnetic resonance analyses," *Magn. Reson. Chem.*, vol. 59, no. 9–10, pp. 975–990, Sep. 2021, doi: 10.1002/mrc.5141.

[59] J. G. Schiffmann, F. Emmerling, I. C. B. Martins, and L. Van Wüllen, "In-situ reaction monitoring of a mechanochemical ball mill reaction with solid state NMR," *Solid State Nucl. Magn. Reson.*, vol. 109, no. June, p. 101687, Oct. 2020, doi: 10.1016/j.ssnmr.2020.101687.

[60] A. P. M. Kentgens and R. Verhagen, "Advantages of double frequency sweeps in static, MAS and MQMAS NMR of spin I=3/2 nuclei," *Chem. Phys. Lett.*, vol. 300, no. 3–4, pp. 435–443, Feb. 1999, doi: 10.1016/S0009-2614(98)01402-X.

[61] D. Iuga, H. Schäfer, R. Verhagen, and A. P. M. Kentgens, "Population and Coherence Transfer Induced by Double Frequency Sweeps in Half-Integer Quadrupolar Spin Systems," *J. Magn.*

Reson., vol. 147, no. 2, pp. 192–209, Dec. 2000, doi: 10.1006/jmre.2000.2192.

[62] R. Siegel, T. T. Nakashima, and R. E. Wasylishen, "Signal-to-noise enhancement of NMR spectra of solids using multiple-pulse spin-echo experiments," *Concepts Magn. Reson. Part A*, vol. 26A, no. 2, pp. 62–77, Jul. 2005, doi: 10.1002/cmr.a.20038.

[63] A. Brinkmann and A. P. M. Kentgens, "Proton-Selective ^{17}O−H Distance Measurements in Fast Magic-Angle-Spinning Solid-State NMR Spectroscopy for the Determination of Hydrogen Bond Lengths," *J. Am. Chem. Soc.*, vol. 128, no. 46, pp. 14758–14759, Nov. 2006, doi: 10.1021/ja065415k.

[64] D. Massiot *et al.*, "Modelling one- and two-dimensional solid-state NMR spectra," *Magn. Reson. Chem.*, vol. 40, no. 1, pp. 70–76, Jan. 2002, doi: 10.1002/mrc.984.

[65] C. J. Jameson, "Reply to `conventions for tensor quantities used in nuclear magnetic resonance, nuclear quadrupole resonance and electron spin resonance spectroscopy," *Solid State Nucl. Magn. Reson.*, vol. 11, no. 3–4, pp. 265–268, Jun. 1998, doi: 10.1016/S0926-2040(98)00029-0.

[66] G. Kresse and J. Hafner, "Ab initio molecular-dynamics simulation of the liquid-metal–amorphous-semiconductor transition in germanium," *Phys. Rev. B*, vol. 49, no. 20, pp. 14251–14269, May 1994, doi: 10.1103/PhysRevB.49.14251.

[67] P. Giannozzi *et al.*, "QUANTUM ESPRESSO: a modular and open-source software project for quantum simulations of materials," *J. Phys. Condens. Matter*, vol. 21, no. 39, p. 395502, Sep. 2009, doi: 10.1088/0953-8984/21/39/395502.

[68] S. Baroni, S. de Gironcoli, A. Dal Corso, and P. Giannozzi, "Phonons and related crystal properties from density-functional perturbation theory," *Rev. Mod. Phys.*, vol. 73, no. 2, pp. 515–562, Jul. 2001, doi: 10.1103/RevModPhys.73.515.

[69] J. P. Perdew, K. Burke, and M. Ernzerhof, "Generalized Gradient Approximation Made Simple," *Phys. Rev. Lett.*, vol. 77, no. 18, pp. 3865–3868, Oct. 1996, doi: 10.1103/PhysRevLett.77.3865.

[70] N. Troullier and J. L. Martins, "Efficient pseudopotentials for plane-wave calculations," *Phys.*

Rev. B, vol. 43, no. 3, pp. 1993–2006, Jan. 1991, doi: 10.1103/PhysRevB.43.1993.

[71] L. Kleinman and D. M. Bylander, "Efficacious Form for Model Pseudopotentials," *Phys. Rev. Lett.*, vol. 48, no. 20, pp. 1425–1428, May 1982, doi: 10.1103/PhysRevLett.48.1425.

[72] C. J. Pickard and F. Mauri, "All-electron magnetic response with pseudopotentials: NMR chemical shifts," *Phys. Rev. B*, vol. 63, no. 24, p. 245101, May 2001, doi: 10.1103/PhysRevB.63.245101.

[73] K. Lejaeghere *et al.*, "Reproducibility in density functional theory calculations of solids," *Science*, vol. 351, no. 6280, p. 1415, Mar. 2016, doi: 10.1126/science.aad3000.

[74] L. Stievano *et al.*, "Density Functional Theory Modeling and Calculation of NMR Parameters: An ab Initio Study of the Polymorphs of Bulk Glycine," *Cryst. Growth Des.*, vol. 10, no. 8, pp. 3657–3667, Aug. 2010, doi: 10.1021/cg100525h.

[75] H. Colas *et al.*, "Whewellite, $CaC_2O_4 \cdot H_2O$: structural study by a combined NMR, crystallography and modelling approach," *CrystEngComm*, vol. 15, no. 43, p. 8840, 2013, doi: 10.1039/c3ce41201f.

[76] P. Pyykkö, "Year-2017 nuclear quadrupole moments," *Mol. Phys.*, vol. 116, no. 10, pp. 1328–1338, May 2018, doi: 10.1080/00268976.2018.1426131.

[77] T. Friščić, S. L. Childs, S. A. A. Rizvi, and W. Jones, "The role of solvent in mechanochemical and sonochemical cocrystal formation: a solubility-based approach for predicting cocrystallisation outcome," *CrystEngComm*, vol. 11, no. 3, pp. 418–426, 2009, doi: 10.1039/B815174A.

[78] G. A. Bowmaker, "Solvent-assisted mechanochemistry," *Chem. Commun.*, vol. 49, no. 4, pp. 334–348, 2013, doi: 10.1039/C2CC35694E.

[79] C. A. Téllez S, E. Hollauer, M. A. Mondragon, and V. M. Castaño, "Fourier transform infrared and Raman spectra, vibrational assignment and ab initio calculations of terephthalic acid and related compounds," *Spectrochim. Acta Part A Mol. Biomol. Spectrosc.*, vol. 57, no. 5, pp. 993–

1007, Apr. 2001, doi: 10.1016/S1386-1425(00)00428-5.

[80] R. K. Harris, R. E. Wasylishen, and M. J. Duer, *NMR Crystallography*. Chichester, UK: John Wiley & Sons, Ltd, 2009.

[81] D. L. Bryce, "NMR crystallography: structure and properties of materials from solid-state nuclear magnetic resonance observables," *IUCrJ*, vol. 4, no. 4, pp. 350–359, Jul. 2017, doi: 10.1107/S2052252517006042.

[82] M. E. Smith, "Recent progress in solid-state nuclear magnetic resonance of half-integer spin low-γ quadrupolar nuclei applied to inorganic materials," *Magn. Reson. Chem.*, vol. 59, no. 9–10, pp. 864–907, Sep. 2021, doi: 10.1002/mrc.5116.

[83] C. Leroy, P. M. J. Szell, and D. L. Bryce, "On the importance of accurate nuclear quadrupole moments in NMR crystallography," *Magn. Reson. Chem.*, vol. 57, no. 5, pp. 265–267, May 2019, doi: 10.1002/mrc.4787.

[84] C. Leroy and D. L. Bryce, "Recent advances in solid-state nuclear magnetic resonance spectroscopy of exotic nuclei," *Prog. Nucl. Magn. Reson. Spectrosc.*, vol. 109, pp. 160–199, Dec. 2018, doi: 10.1016/j.pnmrs.2018.08.002.

[85] J. C. Johnston, R. J. Iuliucci, J. C. Facelli, G. Fitzgerald, and K. T. Mueller, "Intermolecular shielding contributions studied by modeling the ^{13}C chemical-shift tensors of organic single crystals with plane waves," *J. Chem. Phys.*, vol. 131, no. 14, p. 144503, Oct. 2009, doi: 10.1063/1.3225270.

[86] ECATIO, "No information for the experimental collection of the X-ray diffraction data could be found for the CCDC structure ECATIO."

[87] F. Pourpoint *et al.*, "Calcium Phosphates and Hydroxyapatite: Solid-State NMR Experiments and First-Principles Calculations," *Appl. Magn. Reson.*, vol. 32, no. 4, pp. 435–457, Dec. 2007, doi: 10.1007/s00723-007-0040-1.

[88] M. Reinholdt *et al.*, "Synthesis and Characterization of Crystalline Structures Based on

Phenylboronate Ligands Bound to Alkaline Earth Cations," *Inorg. Chem.*, vol. 50, no. 16, pp. 7802–7810, Aug. 2011, doi: 10.1021/ic200961a.

[89] S. Sene *et al.*, "Boronate Ligands in Materials: Determining Their Local Environment by Using a Combination of IR/Solid-State NMR Spectroscopies and DFT Calculations," *Chem. - A Eur. J.*, vol. 19, no. 3, pp. 880–891, Jan. 2013, doi: 10.1002/chem.201203560.

[90] V. Martins *et al.*, "^{17}O solid-state NMR at ultrahigh magnetic field of 35.2 T: Resolution of inequivalent oxygen sites in different phases of MOF MIL-53(Al)," *Magn. Reson. Chem.*, vol. 59, no. 9–10, pp. 940–950, Sep. 2021, doi: 10.1002/mrc.5122.

[91] T. D. Bennett *et al.*, "Connecting defects and amorphization in UiO-66 and MIL-140 metal–organic frameworks: a combined experimental and computational study," *Phys. Chem. Chem. Phys.*, vol. 18, no. 3, pp. 2192–2201, 2016, doi: 10.1039/C5CP06798G.

[92] U. Johansson, R. L. Frost, W. Forsling, and J. T. Kloprogge, "Raman Spectroscopy of the Kaolinite Hydroxyls at 77 K," *Appl. Spectrosc.*, vol. 52, no. 10, pp. 1277–1282, Oct. 1998, doi: 10.1366/0003702981942780.

[93] B. Kolesov, "Raman investigation of H_2O molecule and hydroxyl groups in the channels of hemimorphite," *Am. Mineral.*, vol. 91, no. 8–9, pp. 1355–1362, Aug. 2006, doi: 10.2138/am.2006.2179.

[94] M. Yang *et al.*, "Near Infrared Spectroscopic Study of Trioctahedral Chlorites and Its Remote Sensing Application," *Open Geosci.*, vol. 11, no. 1, pp. 815–828, Nov. 2019, doi: 10.1515/geo-2019-0063.

[95] H. T. Flakus, B. Hachuła, J. T. Hołaj-Krzak, F. A. Al-Agel, and N. Rekik, "'Long-distance' H/D isotopic self-organization phenomena in scope of the infrared spectra of hydrogen-bonded terephthalic and phthalic acid crystals," *Spectrochim. Acta Part A Mol. Biomol. Spectrosc.*, vol. 173, pp. 65–74, Feb. 2017, doi: 10.1016/j.saa.2016.08.051.

[96] S. Lukin *et al.*, "Isotope Labeling Reveals Fast Atomic and Molecular Exchange in

Mechanochemical Milling Reactions," *J. Am. Chem. Soc.*, vol. 141, no. 3, pp. 1212–1216, Jan. 2019, doi: 10.1021/jacs.8b12149.